Planes of Satellite Galaxies in Large-scale Cosmological Simulations

Pascal Ulrich Förster

Munich 2019

Planes of Satellite Galaxies in Large-scale Cosmological Simulations

Master's thesis

at the

Ludwig–Maximilians–Universität in Munich

handed in by

Pascal Ulrich Förster

(Matr. No.: 8052487)

born December 5, 1987 in Düsseldorf, Germany

supervised by
PD Dr. Klaus Dolag

and
Dr. Rhea-Silvia Remus

Munich, March 14, 2019

Evaluator: PD Dr. Klaus Dolag

Satellitengalaxienebenen in großskaligen kosmologischen Simulationen

Masterarbeit

an der

Ludwig–Maximilians–Universität München

eingereicht von

Pascal Ulrich Förster

(Matr.-Nr.: 8052487)

geboren am 5. December 1987 in Düsseldorf, Deutschland

betreut von
PD Dr. Klaus Dolag

und

Dr. Rhea-Silvia Remus

München, den 14. März 2019

Gutachter: PD Dr. Klaus Dolag

Table of Contents

Observations always involve theory.
— Edwin P. Hubble, the realm of the nebulae

Antique philosophers and medieval astronomers based their theories of our cosmos, as bounded as they may seem to us nowadays, upon a strong belief in order. The well ordered solar system, neatly divided into harmonic shells rotating within each other, represented a highly mechanistic and "perfectionistic" expectation towards the cosmos.

Modern astronomy has broken these chains of anthropocentrism, but the search for the bigger picture, the imprint of the cosmos unto us and our environment remains. This thesis is no exception.

Summary

The thesis at hand has been prompted by recent observations of highly anisotropic distributions of dwarf satellite galaxies around nearby central galaxies. We start this thesis with an overview of current observations of planes of satellite galaxies: the three central galaxies, for which sufficient and reliable data could be gathered, are our neighbor Andromeda, the Milky Way, and Centaurus A, an elliptical galaxy of about $10^{12}\,\mathrm{M}_\odot$.

All three of them have been observed to feature a thin plane of satellites that is highly anisotropic and statistically significant; estimates of possible chance occurrences of a single such plane are usually well below 1%, so the odds for three similarly significant planes are negligible. Subsequent searches in cosmological simulations have led to mixed results, which makes our search in MAGNETICUM even more intriguing.

In order to try and find explanations of this pronounced anisotropy in a universe that is presumed to be mostly isotropic on large scales, we explore three formation scenarios for such planes and briefly assess them for their feasibility: group infall, second-generation tidal dwarfs, and filamentary accretion. Each of them has their merits, and each of them has their caveats, but filamentary accretion seems to align itself best with the concept of hierarchical structure formation.

Proceeding from these theoretical and observational considerations, we develop two methods of identification of satellite alignment and planes. The first approach, called *three-satellite planes* method, tries to locate preferential alignment through searches among all possible combinations involving three satellites of the respective central purely based on their positions. The second approach, the *momentum in thinnest plane* method, fits the thinnest possible planes to subsets of the satellite population of a galaxy, and then checks if their momentum adheres reasonably well to these planes.

The key results of our study are as follows: we find a pronounced preference for thin, momentum-aligned planes in the ensemble of our more than 600 systems. This trend is most visible in planes consisting of up to 50% of the satellites available in the system, but also carries on into planes with a higher fraction of satellites partaking. Further study is needed to quantitatively compare to other simulations and observations, but the results are nonetheless promising.

1 A short introduction to satellite galaxies

1.1 Observations of satellite galaxy planes

The history of observations of satellite galaxies is tightly linked to that of two well-known specimen: the Large (LMC) and the Small Magellanic Cloud (SMC). First documented observations reach as far back as to the 9th century, when Western Asian scholars like Ibn Qutaybah and later Al Sufi mentioned them in their descriptions of the stars. But since they are visible only from the Southern Hemisphere, it took the so-called Age of Discovery and the arrival of the 16th century for reports of them to reach Europe.

In recent years, the Lambda Cold Dark Matter (ΛCDM) model of cosmological structure formation, as described in e.g. Liddle (2015), has been called into question by what has subsequently been dubbed "the planes of satellite galaxies problem" by Pawlowski (2018) and others. The anisotropic distribution of dwarf satellite galaxies of nearby systems was identified as a problem for ΛCDM by Kroupa et al. (2005), although this general claim was contested by Zentner et al. (2005) and Libeskind et al. (2005) even at the time.

In the remainder of this section, we will take at look at some prominent observations of planes of satellites around central galaxies as well as prior searches for similar structures in cosmological simulations.

1.1.1 Milky Way, Andromeda and Centaurus A

The three most prominent planes of satellites around central galaxies are located in our vicinity: the *Vast Polar Structure* (VPOS) around the Milky Way (MW), described by Kroupa et al. (2005) and Pawlowski et al. (2012); the *Great Plane of Andromeda* (GPoA) around M31, found by Conn et al. (2012) and Ibata et al. (2013); and the *Centaurus A Satellite Plane* (CASP) around NGC 5128, established by Tully et al. (2015) and Müller et al. (2016).

While the anisotropy around our MW has been suspected for quite some time (cf. Lynden-Bell 1976, Kunkel and Demers 1976), only newer, more complete surveys and significant advances in observation techniques were able to settle the matter. Large-

Figure 1.1: Centaurus A, a neighboring elliptical galaxy at ≈ 3.8 Mpc distance. Image credit: HST+ESO/Robert Gendler+Roberto Colombari

Figure 1.2: The Large and the Small Magellanic Clouds as seen from Paranal Observatory in Chile. Image Credit: ESO/John Colosimo
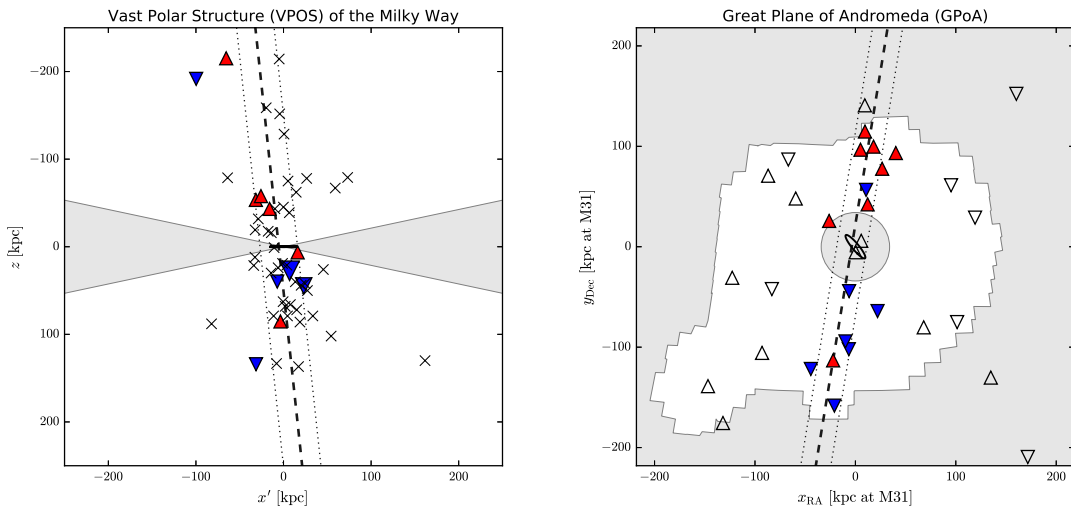
Figure 1.3: Observations of the Milky Way and Andromeda planes of satellite galaxies in edge-on view. *Left:* the VPOS of the MW as it would be seen from a position with both in edge-on view. *Right:* the GPoA around Andromeda as seen from the Sun. In both plots, the best fitted satellite galaxy planes are displayed as dashed lines with their respective width included as dotted lines. Where available, satellite velocities are shown as blue downward triangles for approaching and red upward triangles for receding satellites that are part of the plane, and as open triangles for those that are not part of the plane. Crosses mark satellites for which no individual velocities are available. The shaded areas mark regions with severe observational limitations. Figure taken from Pawlowski (2018).

scale surveys of nearby galaxies such as the Pan-Andromeda Archaeological Survey (PAndAS, McConnachie et al. 2009) for M31 and the Dark Energy Camera (DECam, Müller et al. 2017) for the Centaurus group have expanded the search beyond our own galaxy, and with both the GPoA around Andromeda and the CASP around the more distant Centaurus A, further examples of highly anisotropic constellations of satellite galaxies have been discovered. The current findings are shown in Figure 1.3 for the MW and M31, and in Figure 1.4 for Centaurus A.

Statistics

It is important to note that these planes of satellites are statistically highly significant, as shown by Pawlowski (2016). The Sloan Digital Sky Survey (SDSS, York et al. 2000) and the Dark Energy Survey (DES, The Dark Energy Survey Collaboration 2005) increased the number of known satellites of the Milky Way from 11 to about 40, and due to their very good alignment with the VPOS of the classical satellites, the significance of the "new" VPOS has increased to $\sigma \approx 4.6$, as calculated
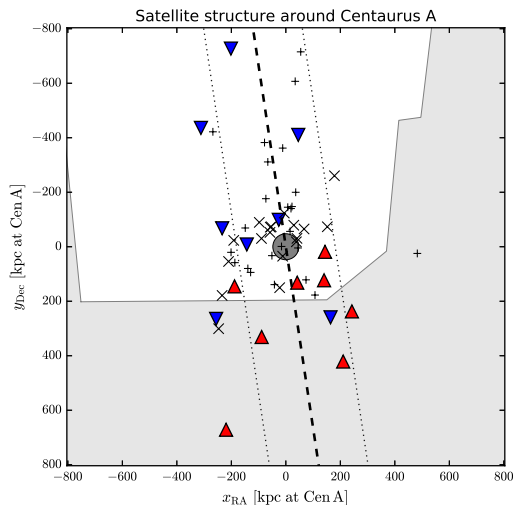
Figure 1.4: Observation of the Centaurus A satellite plane (CASP) in edge-on view. The best fitted satellite galaxy plane is displayed as a dashed line with its respective width included as a dotted line. Where available, satellite velocities are shown as blue downward triangles for approaching and red upward triangles for receding satellites that are part of the plane, crosses mark satellites for which no individual velocities are available. The shaded areas mark regions with severe observational limitations. Figure taken from Pawlowski (2018).

by Pawlowski (2016). The latter corresponds to a probability of $P = 4.3 \cdot 10^{-6}$ to find a configuration that is at least this extreme in a random distribution of satellite galaxies, which in turn very strongly points to relevant, anisotropic formation pathways of these planes.

1.1.2 Previous searches in simulations

Previous searches in simulations have lead to mixed results: while some studies found no planes of comparable statistical importance in neither the MILLENIUM II nor the ILLUSTRIS or the ELVIS simulations (Pawlowski et al. 2014, Pawlowski and McGaugh 2014, Müller et al. 2018), others found strong indications for corresponding satellite galaxy structures, for example Welker et al. (2018) in HORIZON-AGN and Dong et al. (2014) in their own cosmological simulation.

Figure 1.5 shows exemplary comparisons between the significance of the Centaurus A plane of satellites and those of comparable systems in both the MILLENIUM II and the ILLUSTRIS simulations from Müller et al. (2018). With both the flatness
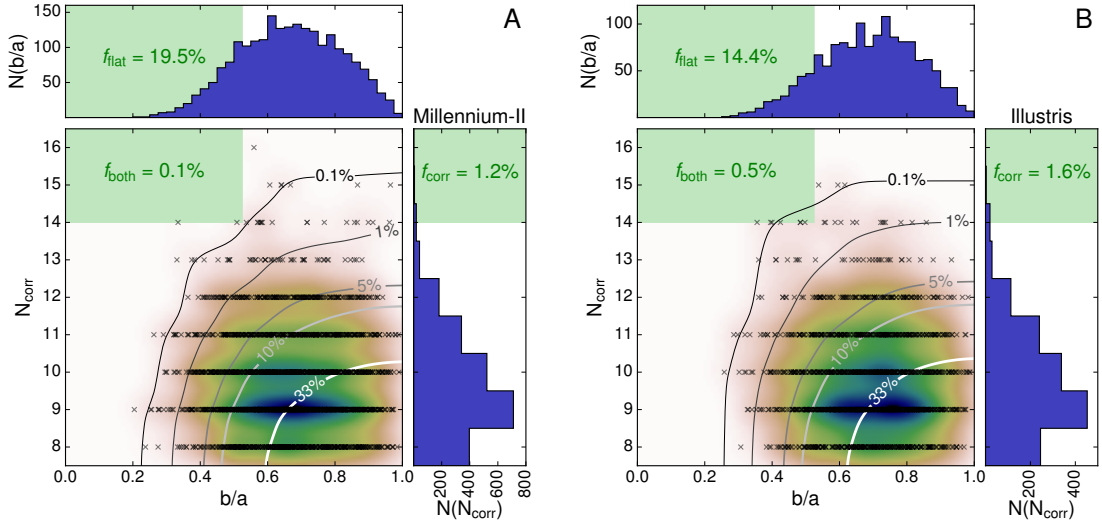
Figure 1.5: Comparison of the Millennium II (*left*) and Illustris (*right*) simulations with the Centaurus A Satellite Plane. Displayed are the number of kinematically correlated satellites N_{corr} over the on-sky axis ratio b/a. The color gradient represents the density of simulated systems for either simulation, with the contour lines indicating the frequency of realization of more extreme – i.e. thinner and kinetically stronger correlated – systems. The histograms show the number of systems within certain axis ratio and velocity correlation bins, respectively. The green shaded regions indicate the frequency of systems that are at least as flat (f_{flat}) or at least as kinetically correlated (f_{corr}) as CASP, but the frequency of systems that fulfill both is only $f_{both} = 0.1\%$ for Millenium II and $f_{both} = 0.2\%$ for Illustris. Figure taken from Müller et al. (2018).

of the plane and the kinematic correlation of its satellites taken into account, the frequencies of realizations of satellite planes with at least the same significance, f_{both}, are well below 1% of Centaurus A analogs in either of the simulations.

1.2 About the formation of planes of satellite galaxies

There are three major scenarios suggested for the formation of the observed, thin planes of satellite galaxies around central host galaxies, which are displayed in Figure 1.6: first, the preferential accretion of dwarf galaxies along the ridge of a filament; second, the accretion of dwarf galaxies in groups; and lastly, the formation of second-generation tidal dwarf galaxies out of the interaction of the tails of two galaxies. All of these scenarios have their advantages and disadvantages, which we will briefly discuss next.
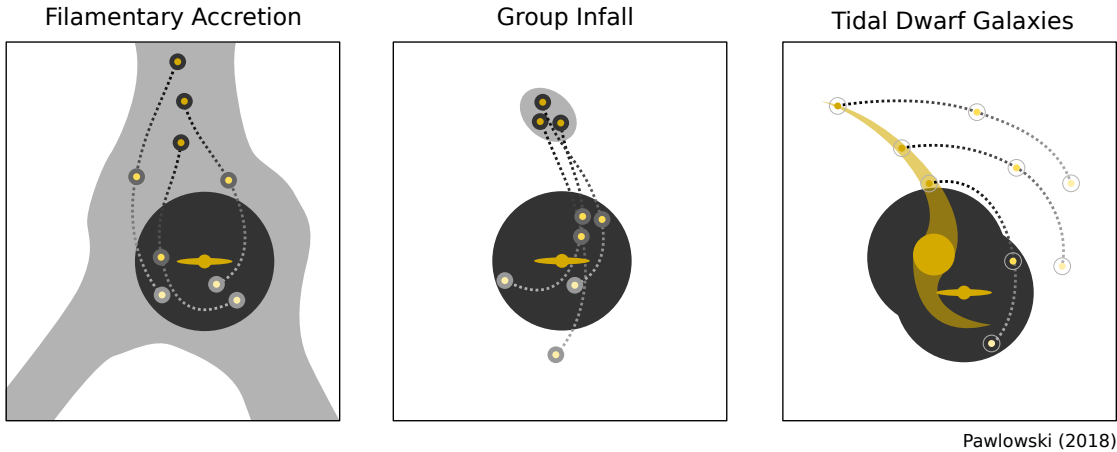
Figure 1.6: Three different formation scenarios for thin planes of satellite galaxies. *Left*: accretion of dwarf galaxies along a filament onto the halo of the central galaxy. *Middle*: group accretion of dwarf galaxies. *Right*: second-generation tidal dwarf galaxies formed from tails of interacting galaxies. Figure taken from Pawlowski (2018)

1.2.1 Filamentary accretion

The accretion of satellites from nearby filaments (Figure 1.6, left panel) is a scenario that is consistent with cosmological observations of the filamentary structure of the universe. Figure 1.7 shows the different stages of central galaxy evolution and satellite accretion according to Welker et al. (2017), which we describe below. The numbering in Figure 1.7, from 11 through 14, represents the different steps in galaxy evolution designated by the typical mass of such a halo in units of $\log_{10}(M/M_\odot)$.

1. In this picture, potential central galaxies form off-side the ridge of the filaments in quadrants of tidal torques that surround the ridge. The polarity of the circumfilament medium results in a galaxy spin that is aligned with the ridge of the nearby filament. Typical halo mass: $10^{11} M_\odot$

2. As the galaxy moves closer to the ridge of the filament and advances along it, its halo grows from anisotropic filamentary accretion, and the specific angular momentum starts to change due to it. Typical halo mass: $10^{12} M_\odot$

3. The continuing accretion and mergers with dwarf galaxies that travel in the direction of filamentary flow further increase the halo mass and size. The stretching along the filament axis as well as the transfer of their momentum finally flips the specific angular momentum orthogonally to the filament. The rotation plane of the central galaxy slowly follows suit. Typical halo mass: $10^{13} M_\odot$
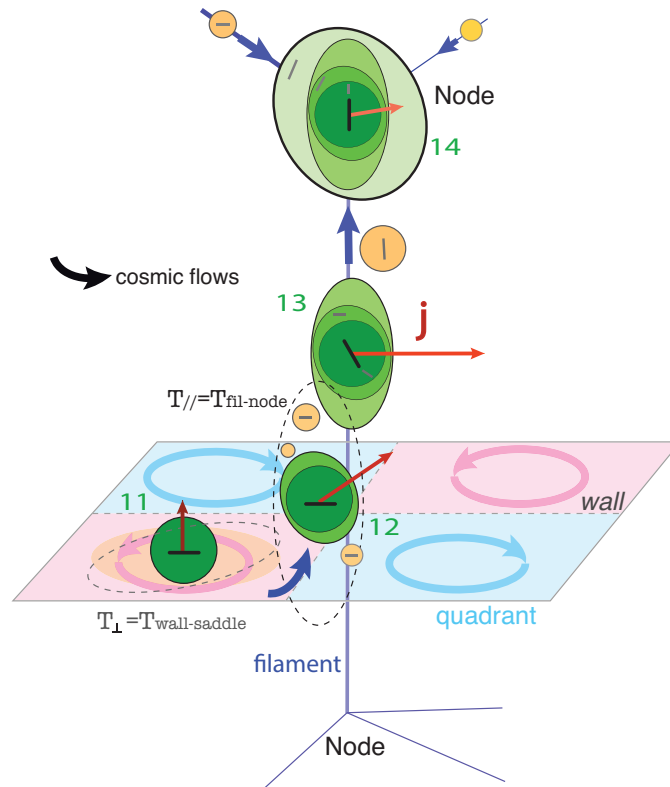
Figure 1.7: Different stages of central galaxy evolution and satellite galaxy accretion. The designated central galaxy is shown through its disk (black bar) and specific angular momentum (red to orange arrow) within its growing halo (green ellipsoids) during four steps of its evolution along the ridge of the filament (blue vertical line). The dwarf and later to be satellite galaxies are displayed as orange halos with grey bars. The massive, dark blue arrows represent the filamentary flow, and the light blue and pink shaded regions with circular arrows of the same color indicate the preferred rotation of the circumfilament medium in each quadrant. For a more detailed description of the evolution, please see the text in Section 1.2.1. Figure taken from Welker et al. (2017)

4. Finally, the halo with its central galaxy and accreted satellites settles in a cosmic node, its rotation in direction of its original filament, but its specific angular momentum again less pronounced due to the now multidirectional infall. Typical halo mass: $10^{14} M_\odot$

Some authors (e.g. Pawlowski 2018) argue that at the time of satellite accretion, the filaments are wider than the hosts virial radii. The solution to this problem is already included in the above refined evolution scheme, though: the preferential accretion of massive halos along the spines of filaments allows the infall of dwarf galaxies to be sufficiently anisotropic to produce thin planes of coherently moving satellites. Even better, this effect follows directly from the hierarchical structure formation of ΛCDM and requires no significant adjustments to the cosmological model. Another advantage of the filamentary accretion scenario is that it represents a somewhat steady, prolonged process that is independent of single, statistically less likely events the two scenarios described below depend upon.

1.2.2 Group infall

The accretion of satellites from a common, infalling group of dwarf satellites is another suggested formation scenario for galaxy satellite planes (Figure 1.6, middle panel). In this case, satellites would fall into the halo of the host galaxy in a small group and thus share orbital orientation, energy and specific angular momentum (Lynden-Bell and Lynden-Bell 1995). It is then expected that the tidal forces of the host halo will disrupt the initially bound satellites and disperse them along their common orbital plane around the central galaxy.

The main problem with the group infall scenario is that in order for the resulting satellite planes to be sufficiently narrow, the accreted groups of dwarf satellites need to be very compact to start with. In contrast, observations of the local Universe find such associations to be much more extended, with their size on the order of 200kpc as opposed to satellite planes with a thickness of $15 - 30$kpc (Metz et al. 2009).

What further disqualifies the group infall scenario as the main formation scenario for the planes of satellites is, that either aforementioned groups would have to consist of a larger LMC-equivalent and a sizable number of smaller companions – enough to populate the whole plane –, or that several smaller groups of dwarf satellites would have to be accreted individually but with very similar infall characteristics. While the latter leads back to the filamentary infall of the previous Section 1.2.1, the former is strongly discouraged by numerical simulations with regard to both the number of dwarf galaxies per group (Li and Helmi 2008, Wang et al. 2013, Wetzel et al. 2015, Shao et al. 2018) and to the ability to populate all observed regions of a plane around the host (Nichols et al. 2011, Angus et al. 2016).

1.2.3 Tidal dwarfs

The third formation scenario for planes of satellite galaxies centers around second-generation tidal dwarf galaxies, as shown in the right panel of Figure 1.6. They have been observed to form in the aftermath of the interaction between two larger galaxies, when the debris collapses under self-gravity. In terms of properties like size, mass, and star formation rate, they very much resemble normal dwarf galaxies (Weilbacher et al. 2000, Wetzstein et al. 2007), and since all tidal dwarfs form out of a common tidal tail, they share the same orbital plane and direction (Kroupa 2012, Hammer et al. 2013). Furthermore, Ploeckinger et al. (2018) have reported the formation of tidal dwarf candidates in the ΛCDM simulation EAGLE.

The major reservations towards second-generation tidal dwarfs with regards to planes of satellite galaxies stems from one of their key characteristics: due to their formation history, tidal dwarf galaxies should be mostly dark matter free, but their best candidates in the Local Group (LG), the dwarf spheroidal galaxies (dSph), are observed to be highly dark matter dominated[1] according to ΛCDM. The proposed solutions to this conundrum are, by and large, deeply dissatisfying: one would have to either question the validity of the observations or the dSphs assumed equilibrium (Metz and Kroupa 2007), modify the properties of dark matter to enable participation in tidal dwarf galaxy formation (Foot and Silagadze 2013, Randall and Scholtz 2015), or switch from ΛCDM to a modified gravity framework altogether.

None of the above solutions to the second-generation tidal dwarfs' observation-vs-prediction problem can alleviate the more general problems associated with attributing a seemingly widespread commodity like planes of satellite galaxies to single event formation scenarios. The latter would require a frequency of order near unity for galaxy-galaxy interactions resulting in tidal dwarfs, while having only minimal scatter towards several encounters, which would lead to multiple planes or more isotropic satellite configurations.

---

[1]Measurements of the LG dSphs indicate high velocity dispersions of their luminosities, which in turn leads to a mass-to-light ratio of beyond $M/L = 10\,M_\odot/L_\odot$.

2 Finding satellite planes in simulations

In this section, we will direct our focus to the pressing task of finding and implementing suitable schemes to identify and analyze planes of satellite galaxies around their central galaxies. Our aim is to be complete, but not necessarily pure in the first place, then to further refine the analysis by systematic means while retaining completeness. To this end, we develop two approaches: the "three-satellite planes" (short: TSP) scheme is described in Section 2.1, whereas the second approach via momentum alignment of satellites to their position-wise best fitted, thinnest planes – henceforth called "momentum in thinnest plane" scheme (short: MTP) – is discussed thereafter, in Section 2.2.

2.1 The three-satellite planes scheme

The three-satellite planes scheme (short: TSP) aims to amplify any preference in subhalo alignment in galactic halos of arbitrary configuration. The basic idea for the analysis of single halos in our ensemble is as follows: we permute through all possible combinations of three subhalos in the given halo of satellite number N. Then we construct the normal vectors of all of those distinct planes and, after normalizing them, evaluate them against an axis of our choosing. The distribution of separation angles between all of these normal vectors and the axis for this given system is an indicator for preferential alignment of subhalos. Please see Figure 2.1 for a mock-up visualization of the approach. In the following subsections, we will look at the different aspects of this scheme in more detail.

2.1.1 Constructing all three-satellite planes

Permuting through all possible three-satellite combinations lends us a number of three-satellite planes N_{TSP} that is

$$N_{\mathrm{TSP}} = \binom{N}{3} \, .\tag{2.1}$$

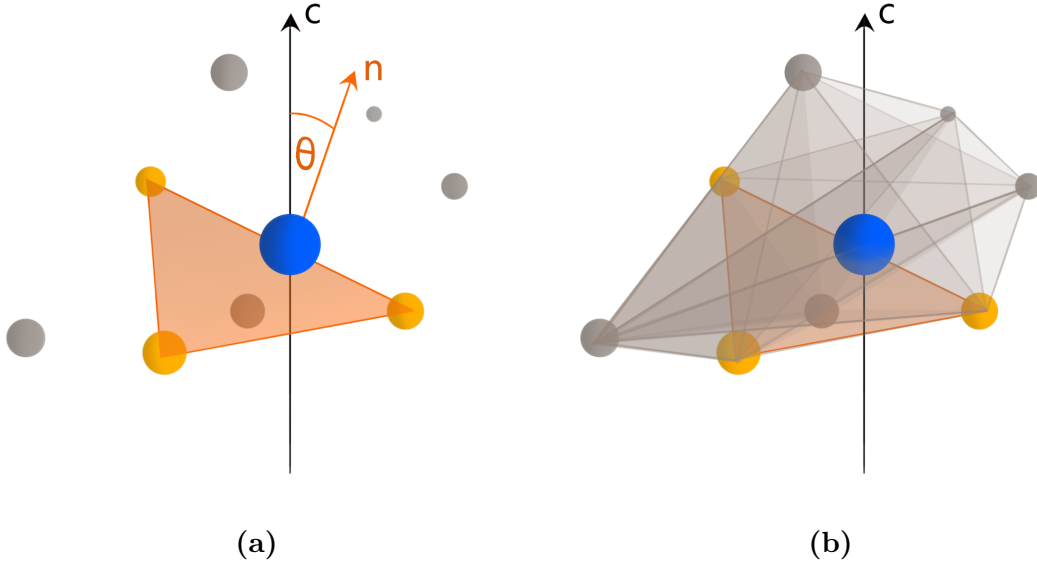**(a)**   **(b)**

Figure 2.1: Sketches of a system consisting of a central galaxy (*blue*)
with the minor axis $\vec{c}$ and its eight satellites. The three satellites that
are part of the specifically highlighted plane (*red* triangle) are colored in
gold, the rest are kept in *gray*. **(a)** Only one plane is shown, together with
its normal vector $\vec{n}$ and the separation angle θ; **(b)** visualization of all
three-satellite planes in the system shown in (a).

To better gauge the order of magnitude of N_{TSP}, we use $\binom{n}{k} = \frac{n!}{k!(n-k)!}$ to simplify
Equation (2.1) and get

$$N_{\mathrm{TSP}} = \frac{N!}{3!(N-3)!} = \frac{N \cdot (N-1) \cdot (N-2)}{6} \; ,$$

which for sufficiently large $N \gg 3$ starts to grow with $\mathcal{O}^3$:

$$N_{\mathrm{TSP}} \approx N^3 \qquad \text{(for } N \gtrsim 30) \qquad\qquad (2.2)$$

It may thus grow prohibitively large for some of the systems in our sample; the
most massive halo, for example, has $N = 1529$ subhalos, which results in a number
of $N_{\mathrm{TSP}} \approx 5.9 \cdot 10^8$ three-satellite planes. As evidenced by Figure 3.2, those very
massive and satellite-rich systems are far from our standard case, though.

Since by definition any three points lie in a plane, every set of three satellites S_α
with $\alpha \in [1, N_{\mathrm{TSP}}]$ will form a plane with a corresponding normal vector

$$\vec{n}_\alpha = \frac{\vec{\eta}_{ijk}}{|\vec{\eta}_{ijk}|} \; , \qquad\qquad (2.3)$$

where $\vec{\eta}_{ijk}$ is the cross product of two out of three possible, linearly independent

separation vectors between the three satellites in this specific set S_α:

$$\vec{\eta}_{ijk} = (\vec{x}_j - \vec{x}_i) \times (\vec{x}_k - \vec{x}_i) \ . \tag{2.4}$$

Here, $\vec{x}_i, \vec{x}_j, \vec{x}_k$ denote the position vectors of the three satellites at hand in set S_α.

2.1.2 Evaluating the three-satellite planes

From there on we continue to evaluate the set of all three-satellite planes as represented by the set of their normal vectors $\{\vec{n}_\alpha\}$ against a single, chosen axis $\vec{q}$. This is done by means of the scalar product of vectors $\vec{n}_\alpha$ and $\vec{q}$, which lends us the cosine of the separation angle θ_α between the two:

$$\cos\theta_\alpha = \vec{n}_\alpha \cdot \vec{q} \ , \quad \text{for all } \alpha \in [1, N_{\text{TSP}}] \tag{2.5}$$

It is reasonable to select an axis of physical meaning for this analysis, such as the spin minor axis[1] of the central galaxy of the halo which we denote with $\vec{c}$. If our coordinate system $\{\vec{x}, \vec{y}, \vec{z}\}$ has previously been aligned with the principal axes of the central galaxy in the halo $\{\vec{a}, \vec{b}, \vec{c}\}$, then Equation (2.5) simplifies to:

$$\cos\theta_\alpha = \vec{n}_\alpha \cdot \vec{c} = \vec{n}_\alpha \cdot \begin{pmatrix} 0 \\ 0 \\ 1 \end{pmatrix} = n_{\alpha,z} \ , \tag{2.6}$$

which is just the z-component of any of the normal vectors $\vec{n}_\alpha$. This is shown in Figure 2.1a. The evaluation is computationally effective especially for the very large numbers of three-satellite planes N_{TSP} that we may encounter on the higher-mass end of our ensemble of halos.

2.1.3 Uniform random distribution on a sphere

Equations (2.5) and (2.6) notably feature the cosine of the separation angle θ instead of the angle itself. It is beneficial for our further analysis to retain it in this form; the reason for this is the nature of the uniform random distribution on a sphere and its reduction from 3D space into a single parameter θ. We will briefly demonstrate this below.

The equivalent of a distribution of unit vectors in three dimensions that are randomly and uniformly oriented in space is to have them start at the origin of coordinates and point onto a unit sphere from within. Then each infinitesimally small surface element of the sphere should have the same number of vectors pointing into

---

[1]The standard convention for naming the principal (semi-)axes of an ellipsoid are a, b, c for the major, intermediate and minor axes, respectively, with $a \geq b \geq c$.

it. Thus, we can transfer the problem from a three-dimensional vector problem to a two-dimensional spherical surface problem. To this end, we first parametrize the surface elements in terms of the polar angle θ and the azimuthal angle ϕ :

$$\mathrm{d}A = r^2 \, \sin\theta \, \mathrm{d}\theta \, \mathrm{d}\phi \tag{2.7}$$

We recognize that for our chosen axis, the z axis, the problem is symmetric under rotation around said axis; thus we do not need to concern ourselves with $\mathrm{d}\phi$ for now and can integrate over its range later. The radius of the unit sphere is $r = 1$, hence we can drop this factor straight away.

Since we want to test the surface element $\mathrm{d}A$ for its dependence on the cosine of θ, we introduce the following notation:

$$\mu \equiv \cos\theta \quad \rightarrow \quad \theta = \arccos\mu \tag{2.8}$$

In order to later on replace $\mathrm{d}\theta$ with some expression depending on μ, we write

$$\mathrm{d}\theta = \mathrm{d}\mu \, \frac{\mathrm{d}\theta}{\mathrm{d}\mu}$$

and use Equation (2.8) and trigonometric relations to reformulate the fraction as

$$\frac{\mathrm{d}\theta}{\mathrm{d}\mu} = \frac{\mathrm{d}\left(\arccos\mu\right)}{\mathrm{d}\mu} = -\frac{1}{\sqrt{1-\mu^2}} \quad .$$

Thus, we can write the initial Equation (2.7) for the surface element $\mathrm{d}A$ in a form entirely parametrized by $\mu = \cos\theta$:

$$\mathrm{d}A = \sin\left(\arccos\mu\right) \frac{-1}{\sqrt{1-\mu^2}} \, \mathrm{d}\mu \, \mathrm{d}\phi \tag{2.9}$$

Using a similar trigonometric relation, namely

$$\sin\left(\arccos\mu\right) = \sqrt{1-\mu^2} \quad ,$$

we are able to simplify Equation (2.9) significantly and obtain

$$\mathrm{d}A = -\, \mathrm{d}\mu \, \mathrm{d}\phi \, . \tag{2.10}$$

This shows that the infinitesimal surface element depends linearly on the $\cos\theta = \mu$, and very much not linearly on θ itself.[2]

---

[2]The surface element $\mathrm{d}A$ also linearly depends on the azimuthal angle ϕ, but since our analysis method (the scalar product with the z axis) is rotationally symmetric, we can integrate over ϕ and replace it by 2π.

Hereby we have shown that the random uniform distribution of vectors in 3D with separation angles θ between them and a chosen axis is a simple horizontal line in a plot over a $\cos\theta$ axis. Since we will judge the significance of preferences in orientation of vectors (read: possible alignment of satellites) by their deviation from the uniform distribution, this result simplifies our task considerably.

Finally, to check the integrity of our derivation, we integrate Equation (2.10) over the whole unit sphere and find that

$$A = \int_{\phi=0}^{2\pi} \int_{\mu=1}^{-1} \mathrm{d}A \; = \int_{\mu=1}^{-1} -2\pi \, \mathrm{d}\mu = \big[-2\pi\big]_1^{-1} = 4\pi \quad,$$

which is – as should be expected – the surface of a sphere with radius 1. $\quad\square$

2.1.4 Symmetry of antiparallel normal vectors

After the short excursion into uniform distributions in the previous section, we continue where we left off after Section 2.1.2. We are interested in uncovering possible preferences in alignment of the subhalos, and to this end we first assert that values of $\theta > 90°$ are equivalent to their $\theta < 90°$ counterparts, since they only reflect antiparallel equivalents of the same normal vectors projected onto an axis $\vec{q}$, and thus the sign of the projection of any normal $\vec{n}_\alpha$ onto our chosen axis $\vec{c}$ (cf. Equation 2.6), $\vec{n}_{\alpha,z}$, is an arbitrary result of the satellite selection process and carries no meaning. This can easily be shown: let $\vec{s}_{2,1}$ and $\vec{s}_{3,1}$ be the separation vectors between satellites 2 and 1 and between satellites 3 and 1, respectively. Then the normal vector of their common plane is given by

$$\begin{aligned}
\vec{n}_{123} &= \vec{s}_{2,1} \times \vec{s}_{3,1} \\
&= -\vec{s}_{3,1} \times \vec{s}_{2,1} = -\vec{n}_{132} \quad,
\end{aligned}$$

which switches sign if we select satellite 2 and 3 in different order, although they clearly make up the same plane as before.

2.1.5 Probability density function and excess probability

Now that the paramter space of $\cos\theta$ in Equation (2.6) is well-defined, we compute the probability to find it within a certain number of bins between 0 and 1. This is best done with a probability density function (PDF) as illustrated in Figure 2.2.

The PDF is plotted as a histogram with five equal-width bins over the interval of $\cos\theta = [0, 1]$ representing angles between 0° and 90°. The uniform distribution on a sphere is displayed as the dashed horizontal line intersecting the ordinate at $y = 1$, and its integral is 1 as should be expected from a probability. Any deviations from
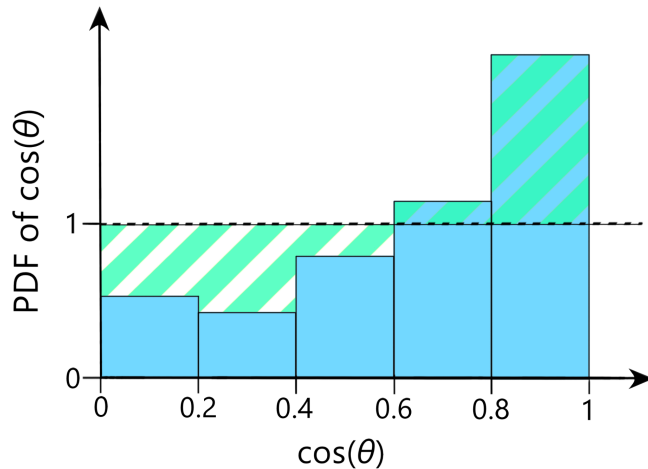
Figure 2.2: Illustration of the probability density function of $\cos\theta$ in five equal-width bins. The area of any individual, *light blue* histogram bar represents the probability to find a value $\mu = \cos\theta_\mu$ in the corresponding bin. The dashed line marks the uniform distribution expected from isotropy, while the *turquoise* shaded regions below and above it are equal in area and represent the excess probability ξ to find μ within these specific bins. In the example at hand, this corresponds to an excess probability of $\xi \approx 24\%$ of finding $\mu \in [0.6,\ 1]$.

the uniform distribution, shaded in turquoise in Figure 2.2, represent an anisotropy in distributions of angles and thus, where the histogram bars reach above the dashed line, an excess probability ξ to find θ in the corresponding interval of $\cos\theta$. In this specific example, the integral of the PDF above the uniform distribution lends us an excess probability of $\xi_{[0.8,\ 1]} \approx 21\%$ to find $\cos\theta$ in the right-most bin, and $\xi_{[0.6,\ 1]} \approx 24\%$ to find it in the two right-most bins.

In general, the excess probability to find $\mu = \cos\theta$ in between the values $0 \le a < b \le 1$ is given by

$$\xi = \int_{\mu=a}^{b} \mathrm{PDF}(\mu)\,\mathrm{d}\mu - 1\ .$$

This is not limited to a histogram PDF but also works for continuous probability densities if the latter are available and their use is deemed feasible.

A short remark about the maximum values of PDFs: the apparent height of any value on the y-axis does not convey much information unless one considers the width of the bin, as the (excess) probabilities are given by the integral of the function and thus the area covered in the plot. The strong dependence of the highest possible

value P_{max} for any PDF with n_{bins} equal-width bins is given by

$$P_{\text{max}} = P_{\text{total}} \cdot n_{\text{bins}} \, ,$$

with $P_{\text{total}} = 1$ the probability over the whole x-range.[3] Since the number of bins in both the example in Figure 2.2 and in our later analysis is $n_{\text{bins}} = 5$, the maximum value is $P_{\text{max}} = 5$ in both.

2.1.6 Combined analysis of many systems

Ultimately, we aim to draw statistical conclusions from our large ensemble of halos. We therefore stack the PDF histograms of different subsets of our halos and look for trends in (excess) probabilities for different $\cos\theta$ bins across the halos of one subset and for differences in trends for the (excess) probabilities for different $\cos\theta$ bins between all subsets. We have considered different splits of the full ensemble, two of the most feasible ones being a split by b-value of the central galaxy and a split by total halo mass. The resulting PDF histograms can be found in Sections 4.1.1 and 4.1.2, respectively.

Possible approaches to analyzing the stacked data are identifying the mean of the probability P for each bin as well as the "scatter" in probability within $\pm 1\sigma$ and $\pm 2\sigma$ of the subsample of halos analyzed. We will perform this for both of the aforementioned split criteria in Section 4.1. Furthermore, we can select systems with prominently high excess probabilities ξ for further study and possibly 3D visualization.

2.2 Momentum in thinnest plane scheme

The momentum in thinnest plane scheme (short: MTP) is as a method independent from the TSP scheme described previously in Section 2.1 of this work, and is applied to every system in our ensemble of $\mathcal{N}_h = 622$ halos individually. Its aim is twofold: for one, in each halo with N subhalos, we search for the thinnest $N - 1$ planes consisting of $n = [2, N]$ subhalos and the central galaxy. In a second step, we compute a measure for the adherence of said n subhalos to their best fit, thinnest plane in terms of their momentum alignment. We will describe both steps in more detail below, the second one starting from Section 2.2.4.

---

[3]In most applications, it stands to reason that the overall probability is 1, but in cases of e.g. dependent probabilities there is the possibility of $P_{\text{total}} \leq 1$.

2.2.1 Distances from a plane

Assuming we have an arbitrarily oriented, mathematical plane p, then this plane can be defined by its normal vector $\vec{n}_p$ and its distance from the origin of the coordinate system d_p. From analytic geometry, we know that the Hesse normal form offers an efficient way to calculate distances from a plane, so we first give its definition as

$$p: \quad \vec{r} \cdot \vec{n}_p - d_p = 0 \ . \tag{2.11}$$

The above equation defines a plane such that all position vectors $\vec{r}$ that satisfy it are part of the plane p. We now remind ourselves that we search for a plane centered around the eponymous central galaxy, so the plane will go through the origin and the distance will be $d_p = 0$. Thus, Equation (2.11) simplifies to

$$p: \quad \vec{r} \cdot \vec{n}_p = 0 \ . \tag{2.12}$$

On the other hand, any satellite S_i at position $\vec{r}_i$ with an orthogonal distance of d_i from the plane p can be imagined as sitting in a plane p_i parallel to p at the distance d_i, giving us a plane

$$p_i: \quad \vec{r}_i \cdot \vec{n}_p - d_i = 0 \ .$$

Therefore, the Hesse normal form offers an efficient way to calculate the distance of any object at position $\vec{r}_i$ via

$$d_i = \vec{r}_i \cdot \vec{n}_p = x_i n_x + y_i n_y + z_i n_z \tag{2.13}$$

The normal vector corresponds to two angles in relation to the coordinate system – and in our case the central galaxy and its minor axis –, the polar angle θ_n and the azimuthal angle ϕ_n in spherical coordinates. We proceed to substitute the polar coordinates

$$n_x = \sin\theta_n \cdot \cos\phi_n \ , \quad n_y = \sin\theta_n \cdot \sin\phi_n \ , \quad n_z = \cos\theta_n$$

in Equation (2.13) so that we obtain

$$d_i = x_i \cdot \sin\theta_n \ \cos\phi_n \ + \ y_i \cdot \sin\theta_n \ \sin\phi_n \ + \ z_i \cdot \cos\theta_n \ .$$

In a final step, we switch from the angles of the normal vector, θ_n and ϕ_n, to the ones describing a vector that lies in the plane p in direction to its highest elevation z-wise. The azimuthal angle $\phi = \phi_n$ stays the same, while the polar angle $\theta = \theta_n - \frac{\pi}{2}$ is turned flat into the plane. Thus,

$$d_i = -x_i \cdot \cos\theta \ \cos\phi \ - \ y_i \cdot \cos\theta \ \sin\phi \ + \ z_i \cdot \sin\theta \tag{2.14}$$

2.2.2 Projecting spherical coordinates onto a grid

Now that we have established a measure for the distance of a satellite from an arbitrarily oriented plane through the central galaxy, let us consider how to project the possible planes onto a sufficiently fine grid for further analysis. Each of these planes $p(\theta, \phi)$ is characterized by a set of two polar angles, θ and ϕ. We will search for the thinnest n-satellite plane after putting all possible values of

$$\theta = \left[0, \frac{\pi}{2}\right] \quad \text{and} \quad \phi = [0, 2\pi]$$

onto a grid with a minimum accuracy a. We define a such that $f = \frac{1}{a}$ is the fraction of the total radius R of the system, meaning we segment the $\pi/2$-length chord of the unit circle along the range of $\theta = [0, \pi/2]$ into a minimum of

$$\kappa = \frac{\pi/2}{f} = \frac{\pi}{2} \cdot a$$

bins. Since we require an integer number of equally spaced bins and do not want to omit the final position at the end of the θ and of the ϕ range, we use

$$k_\theta = \lceil \kappa \rceil + 1 \quad \text{and} \quad k_\phi = 4 \lceil \kappa \rceil + 1 \quad , \tag{2.15}$$

for the number of bins along θ and ϕ. A minimal toy-example is depicted in Table 2.1 and has a very low accuracy of $a = 3$, resulting in $k_\theta = 6$ bins along the polar angle and $k_\phi = 16$ bins along the azimuthal angle. For each of these $N_p = 96$ angle bins, the table shows the thickness of the thinnest n satellite disk, color-coded in gray-scale for simplicity: the darker the shade of gray, the thinner and thus fit-wise better is the plane. The actual technique to find those thinnest planes is discussed in the following section.

It should be noted that for any meaningful application of this analysis, the accuracy a should be set much higher. For example, we later-on use $a = 180$, which corresponds to an angular resolution of at least 0.5°. A table depicting the resulting grid similarly to Table 2.1 would have $N_p = 1133 \cdot 284$ cells, which is why we opt for filled contour plots in Section 4.2.1 of our results.

2.2.3 Finding the thinnest plane

Now that we have established both a measure for the distance of a satellite from an arbitrarily oriented plane through the central galaxy as well as way to rasterize the angles θ and ϕ of potential planes, let us consider a halo with N satellites and a central galaxy. We want to fit a plane containing the central galaxy to an increasing number of n out of the N total number of satellites, starting with $n = 2$, since

ϕ															
1	2	3	4	5	6	7	8	9	10	11	12	13	14	15	16

Table 2.1: Exemplary table depicting a very rough grid of the angles θ and ϕ for all possible planes, with the thickness color-coded grey: darker shades indicate thinner, more favorable planes, lighter shades thicker, less favourable ones. The best fit would be located at ϕ bin 5, θ bin 3.

the central and just one satellite do not form a well defined plane. Beware that there will always be a perfectly fitted, zero-thickness plane containing the central galaxy and *any* $n = 2$ satellites, so which of the $N - 1$ possible "thinnest" planes is selected may depend on chance. In our case, this ambiguity is indeed not accounted for; the selection of the members of the two-satellites-and-one-central plane depends on the index number of our satellite, and thus carries no physical meaning. From $n = 2$ we move upward in number of satellites in steps of one and, for each number $n = 3, 4, \ldots N$, look for the plane $p_n (\theta, \phi)$ through the central that features n out of the total number of satellites N with the smallest maximum distance from p_n.

We compute the thickness of the disc as follows: be $i, j = 1, \ldots, n, \ldots, N$, and $f_{\mathrm{ord}}(\{S_i\}) = \{T_j\}$ a function that orders the set of N satellites $\{S_i\}$ into the set $\{T_j\}$ according to their distance $d_i = d(S_i)$ from a mathematical plane p_n, then the height of the physical plane of satellites P_n is given by

$$D_{p,n} = d\left([f_{\mathrm{ord}}(\{S_i\})]_n\right) = d(T_n) . \tag{2.16}$$

This means we define the thickness of our plane of n satellites by the distance $d_{j=n}$ of the satellite most distant from the plane, but which is still part of it by virtue of being number $j = n$ in distance ordering.

As previously mentioned, we use this method for all $\mathcal{N}_h = 622$ halos in our ensemble, where we go through all $N - 1$ feasible numbers of satellites in a plane n, and for each of these $\sum_{i=0}^{\mathcal{N}_h-1}(N_i - 1)$ cases we compute the thicknesses $D_{n,p}$ of the potential disks of satellites for all the N_p possible planes p on our θ-ϕ grid. Table 2.2 demonstrates this nested approach.

Halo 0			...	Halo $\mathcal{N}_h - 1$		

$n = 2$		
$\theta_1\phi_1$	$\ldots$	$\theta_1\phi_{k_\phi}$
$\vdots$	$\ddots$	$\vdots$
$\theta_{k_\theta}\phi_1$	$\ldots$	$\theta_{k_\theta}\phi_{k_\phi}$

$n = 3$		
$\theta_1\phi_1$	$\ldots$	$\theta_1\phi_{k_\phi}$
$\vdots$	$\ddots$	$\vdots$
$\theta_{k_\theta}\phi_1$	$\ldots$	$\theta_{k_\theta}\phi_{k_\phi}$

$\vdots$

$n = N_0$		
$\theta_1\phi_1$	$\ldots$	$\theta_1\phi_{k_\phi}$
$\vdots$	$\ddots$	$\vdots$
$\theta_{k_\theta}\phi_1$	$\ldots$	$\theta_{k_\theta}\phi_{k_\phi}$

$n = 2$		
$\theta_1\phi_1$	$\ldots$	$\theta_1\phi_{k_\phi}$
$\vdots$	$\ddots$	$\vdots$
$\theta_{k_\theta}\phi_1$	$\ldots$	$\theta_{k_\theta}\phi_{k_\phi}$

$n = 3$		
$\theta_1\phi_1$	$\ldots$	$\theta_1\phi_{k_\phi}$
$\vdots$	$\ddots$	$\vdots$
$\theta_{k_\theta}\phi_1$	$\ldots$	$\theta_{k_\theta}\phi_{k_\phi}$

$\vdots$

$n = N_{\mathcal{N}_h-1}$		
$\theta_1\phi_1$	$\ldots$	$\theta_1\phi_{k_\phi}$
$\vdots$	$\ddots$	$\vdots$
$\theta_{k_\theta}\phi_1$	$\ldots$	$\theta_{k_\theta}\phi_{k_\phi}$

Table 2.2: Schematic overview of the nested scheme used to find the $N_i - 1$ thinnest planes of satellites in all $\mathcal{N}_h$ halos of our ensemble. For more details, please consult Section 2.2.3.

2.2.4 Using velocity planes

In this section, we will explore how to apply the methods developed in Section 2.2.1 to the velocity (and thereby momentum) of satellites. The basic idea is as follows: we take a plane p through the origin of the coordinate system as defined in Equation (2.12). We realize that the velocity $\vec{v}$ of a satellite galaxy that was completely moving in direction of this plane would not only be parallel to said plane p, but – once you shifted it to the origin – geometrically lie in this plane. Thus we adapt Equation 2.12 to read

$$\tilde{p}: \quad \vec{v} \cdot \vec{n}_p = 0 \ ;$$

it gives us $\tilde{p}$, the equivalent of the plane p in velocity space.

Any arbitrary satellite S_i that is not moving in perfect accordance to $\tilde{p}$ will have a velocity vector $\vec{v}_i$ pointing out of said plane, and the distance from this plane in v-space is equivalent to the absolute value of the velocity component perpendicular to the plane, $\vec{v}_{i\perp}$. Therefore, the equivalent to Equation (2.13) for velocities is

$$\tilde{d}_i = \vec{v}_i \cdot \vec{n}_p = v_{i,x}\, n_x + v_{i,y}\, n_y + v_{i,z}\, n_z = |\vec{v}_{i\perp}| \ .$$

For consistency, we substitute n_x, n_y, n_z according to Equation (2.14) and are left with

$$|\vec{v}_{i\perp}| = -v_{i,x} \cdot \cos\theta \, \cos\phi \; - \; v_{i,y} \cdot \cos\theta \, \sin\phi \; + \; v_{i,z} \cdot \sin\theta \ . \qquad (2.17)$$

The above gives us a way to test if a satellite's movement will likely carry him out of the plane p previously fitted according to his and his $n-1$ companion satellites' positions from the current plane selection.

2.2.5 Computing the in-plane momentum fraction

Having found another use of the Hesse normal form in the previous section, we now will apply it to try and characterize the agreement of motion of the n satellites of a previously fitted plane p_n with the latter.

To this end, we first derive the absolute amount of velocity in direction of the plane, $|\vec{v}_{i\parallel}|$, from the linear combination

$$\vec{v}_i = \vec{v}_{i\parallel} + \vec{v}_{i\perp} \, ,$$

and find the fraction of velocity of satellite S_i in direction of the plane to be

$$\tilde{F}_i = \left| \frac{\vec{v}_{i\parallel}}{\vec{v}_i} \right| = \sqrt{1 - \left| \frac{\vec{v}_{i\perp}}{\vec{v}_i} \right|^2} \, . \tag{2.18}$$

We can easily substitute Equation (2.17) in the above equation to actually compute the numerical values, but will keep the shorter notation for readability purposes.

Now, the fraction $\tilde{F}_i$ only applies to one satellite, but this can be easily expanded to combine all n satellites in the plane by means of summation, leading to

$$\tilde{F}_{\{n\}} = \frac{1}{n} \sum_{i=1}^{n} \tilde{F}_i \, .$$

The closer $\tilde{F}_{\{n\}}$ is to 1, the more are the satellites generally aligned with the plane with regard to their motions. This straight forward approach to a cumulative fraction has disadvantages, though: all satellites of the set $\{S_i\}$ are weighted equally, giving the lightest of them the same influence on our measure as the most massive one. To remedy this, we proceed to weigh the satellites by their mass, which effectively makes our new measure $F_{\{n\}}$ the in-plane momentum fraction:

$$F_{\{n\}} = \left(\sum_{i=1}^{n} m_i \, |\vec{v}_{i\parallel}| \right) \bigg/ \left(\sum_{j=1}^{n} m_j \, |\vec{v}_j| \right) \tag{2.19}$$

In a last step, we will now not only compute the in-plane momentum fraction $F_{\{n\}}$ for all n satellites of our fitted n-satellite planes p_n, but also for their subsets with $\eta = 1, \ldots, n$ satellites, selected in decreasing order of their individual fractions $\tilde{F}_i$.

S_i	n satellites						
	S_1	S_2	S_3	S_4	S_5		
$\tilde{F}_i$	0.83	0.99	0.92	0.75	0.89		
1		✓				0.99	
2		✓	✓			0.96	
η 3		✓	✓		✓	0.93	$F_{\{\eta\}}$
4	✓	✓	✓		✓	0.91	
5	✓	✓	✓	✓	✓	0.88	

Table 2.3: Selection scheme for m out of n satellites of the position-wise best fitted plane p_n according to their individual parallel velocity fractions $\tilde{F}_i$, as well as the respective resulting in-plane momentum fractions $F_{\{m\}}$ assuming equal-mass satellites for simplicity.

This will allow us to judge how many of the n satellites the plane p_n was fitted to position-wise actually agree with it momentum- and thus motion-wise. A simplified example of this approach using equal-mass satellites is shown in Table 2.3.

3 Our search for satellite planes in Magneticum

3.1 The Magneticum Pathfinder simulations

3.1.1 About the simulation

The MAGNETICUM PATHFINDER simulations are a set of sophisticated, state-of-the-art hydrodynamical cosmological simulations. They span a wide range of volumes and resolutions, the details of which are given in Tables 3.1 and 3.2. We use *Box4* in the ultra high resolution run – from now on referred to as *Box4/uhr* – to sufficiently resolve the galaxies and their satellites while working with a large enough sample of systems that allows us to draw statistically relevant conclusions.

The simulations were run with an improved developers' version of the N-body/SPH code GADGET-3, which in turn is an updated version of the well-known open-source code GADGET-2 (Springel, 2005). Our updates include but are not limited to the use of better suited kernels as well an improved scheme for artificial viscosity (cf. Beck et al. 2016; Dolag et al. 2005). For a full overview of the methods and techniques employed, please see the first chapter of Teklu (2018) or visit `www.magneticum.org`. For data access via the *Cosmological Web Portal* (Ragagnin et al. 2017), please visit `https://c2papcosmosim.uc.lrz.de`.

3.1.2 Our data set

We use data from *Box4/uhr*, which simulates a cube volume element of the universe with an edge length of $48\,\mathrm{Mpc/h}$ and a very high resolution of $2\cdot576^3$ particles. The simulation consists of the same number of dark matter and gas particles, the former with a mass of $m_{\mathrm{dm}} = 3.6\cdot10^7\,\mathrm{M_\odot/h}$, the latter with $m_{\mathrm{gas}} = 7.3\cdot10^6\,\mathrm{M_\odot/h}$. We are thus able to resolve – among a wide variety of other phenomena – halos containing central galaxies and their satellites, and use their properties like mass, position and velocities in our analysis.

Our sample consists of $\mathcal{N}_h = 622$ halos that have been extracted from *Box4/uhr* at redshift $z = 0.066$ using a version of SUBFIND, an algorithm to identify substructure in cosmological simulations introduced by Springel et al. (2001). As opposed to the
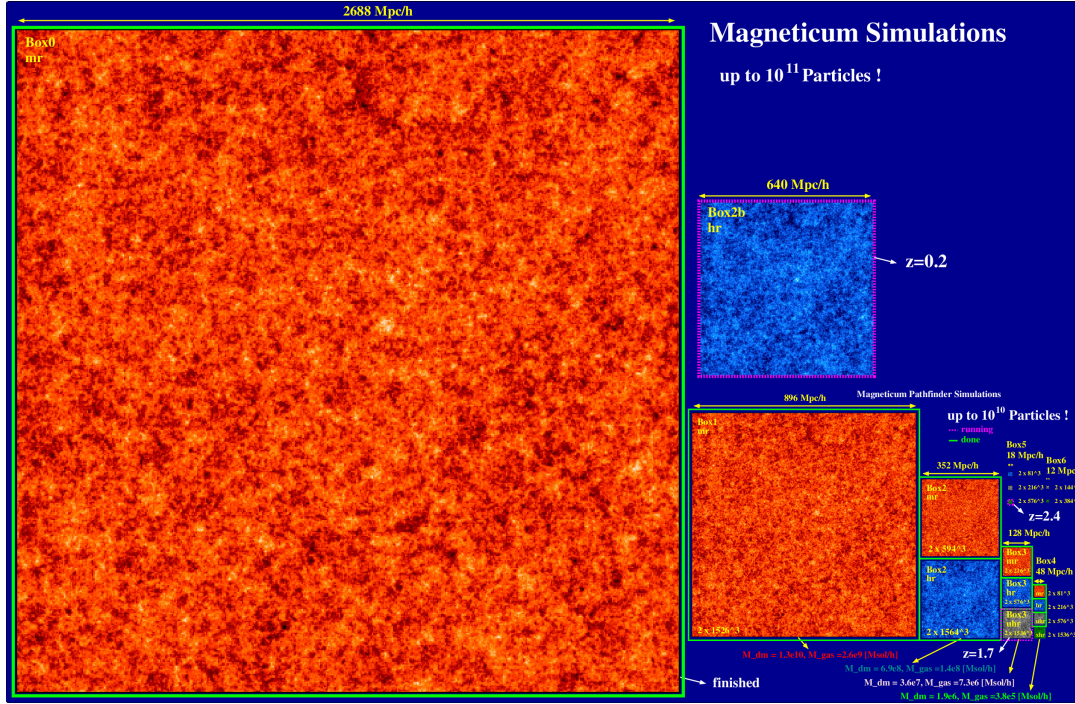
Figure 3.1: Overview of the currently available MAGNETICUM boxes.

Mpc/h	Box0 2688	Box1 896	Box2b 640	Box2 352	Box3 128	Box4 48	Box5 18
mr	$2 \cdot 4536^3$	$2 \cdot 1526^3$		$2 \cdot 594^3$	$2 \cdot 216^3$	$2 \cdot 81^3$	
hr			$2 \cdot 2880^3$	$2 \cdot 1584^3$	$2 \cdot 576^3$	$2 \cdot 216^3$	$2 \cdot 81^3$
uhr					$2 \cdot 1536^3$	$2 \cdot 576^3$	$2 \cdot 216^3$
xhr							$2 \cdot 576^3$

Table 3.1: Number of particles and edge length of the different MAGNETICUM PATHFINDER simulations at their various resolutions levels, *mr*, *hr*, *uhr*, and *xhr*. Listed in gray are currently running simulations.

	m_{dm}	m_{gas}	ϵ_{dm}	ϵ_{gas}	ϵ_{stars}
	M$_\odot$		kpc/h		
mr	$1.3 \cdot 10^{10}$	$2.6 \cdot 10^9$	10	10	5
hr	$6.9 \cdot 10^8$	$1.4 \cdot 10^8$	3.75	3.75	2
uhr	$3.6 \cdot 10^7$	$7.3 \cdot 10^6$	1.4	1.4	0.7
xhr	$1.9 \cdot 10^6$	$3.9 \cdot 10^5$	0.45	0.45	0.25

Table 3.2: Mass of the dark-matter and and gas particles at different resolution levels as well as the softenings employed for dark matter, gas and stars.

central galaxy	color-coding	b-value bins	number of systems
disk	blue	$b > -4.375$	129
intermediate	green	$-4.75 < b \leq -4.375$	188
spheroid	red	$b \leq -4.75$	234

Table 3.3: Color-coding, range of b-values and number of systems for our three b-value bins describing disky, intermediate and spheroidal central galaxies.

original DM-only iteration of the algorithm, our version is modified to encompass both dark matter and baryonic matter according to Dolag et al. (2009). Our systems range from a total halo mass of $M = 7.7 \cdot 10^{11}\,\mathrm{M_\odot}$ on the lower end to very massive halos with large numbers of subhalos and a total mass of $M = 2.3 \cdot 10^{14}\,\mathrm{M_\odot}$ that encroach onto the regime of galaxy clusters.

In Figure 3.2, we display our sample of systems with respect of the total halo mass M over the number of subhalos N of any given system. The systems are color-coded by the b-value, a parameterization of the M_{star}-j_{star} relation by Teklu et al. (2015) based on Romanowsky and Fall (2012), of the central galaxy, giving a good estimate on its general configuration: plotted in blue are the systems with disky centrals, in green the systems with intermediate centrals, and in red the systems hosting spheroidal central galaxies. As evidenced by the monomial-like distribution of markers with exponent 1, the ensemble in its entirety follows a linear relation.[1] The right and upper histograms show the number of systems for each of the three b-value bins in number of mass or number-of-satellite bins, respectively, allowing for a more reliable measure of both quantities where markers get obscured by multiple overlaps in the lower left quadrant of the plot. For an overview of the number of systems in each bin and the corresponding b-values, please see Table 3.3.

3.2 Implementation of our analysis schemes

In this section we describe our implementations of both the "three-satellite planes" scheme introduced in Section 2.1 and the "momentum in thinnest plane" scheme from Section 2.2. Afterwards in Section 3.2.3, we hint at other challenges that arose in the context of implementation.

All code for this analysis was written in Python 3.6 using SciPy, NumPy and Matplotlib. We chose Python as the programming language because it offers high flexibility to adapt to objectives that may shift and evolve during the course of a

---

[1]Monomials as given by $y = c \cdot x^a$ correspond to power laws and, although represented as straight lines in log-log plots, generally do not point to linear but to exponential relations. In our case at hand, though, the ensemble follows a linear relation as evidenced by $a \approx 1$.

Total mass over number of subhalos, colored by b-value
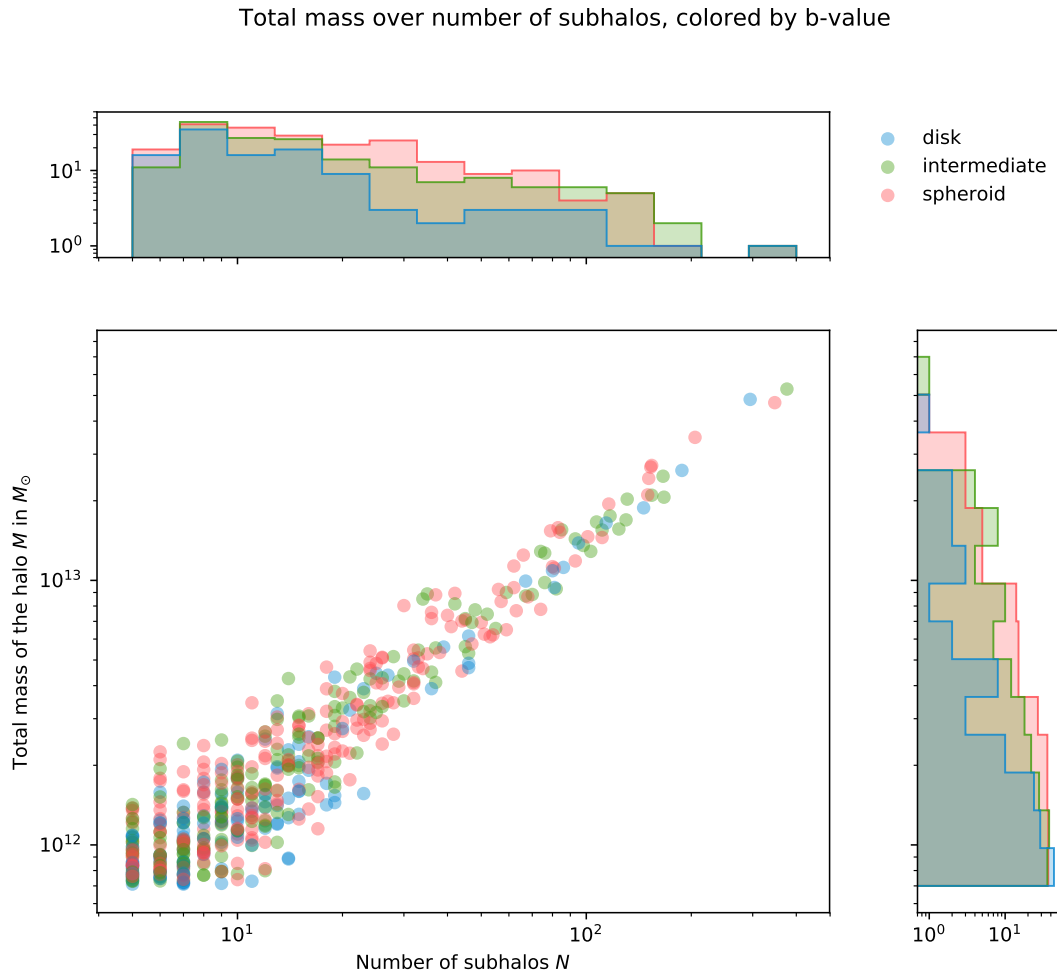
Figure 3.2: The total halo mass M of all systems analyzed with the TSP scheme plotted over their respective number of subhalos N. The sample is split into three bins corresponding to the different b-values of their central galaxies: disk-like (*blue*), intermediate (*green*) and spheroidal (*red*) according to Table 3.3; for more details on the b-value classification please cf. Teklu et al. (2015). The additional panels show histograms of the distribution of N and M, respectively, for the different galaxy types.

thesis. At the same time, we took care to implement our schemes in a reasonably efficient manner, e.g. making frequent use of the inherent parallelization of vectorized array operations in NumPy.

3.2.1 The TSP implementation

The general structure for our implementation of the "three-satellite planes" (TSP) scheme can be summarized in three layers: in layer 1, we iterate over all possible three-satellite combinations, construct their normal vectors and perform a quick analysis. In layer 2, we bin the data from before onto a fine grid for easier handling and to save resources. Finally, in layer 3 we use large number of grids selected according to our criteria and evaluate the accumulated data. We will go into further detail concerning the mostly object-oriented implementation of the different layers below:

Layer 1 - plane normal vector construction

Central design feature of layer 1 is a class called `SHO`. We wrote this "<u>s</u>ub<u>h</u>alo <u>o</u>bject" class in order to retrieve and process the data of each individual halo including its subhalos from their unique data file.

The bulk of each input file consists of a table listing all subhalos and their properties including the central galaxy. Each line is made up of the following information:

```
1  j  x  y  z  vx  vy  vz  mdm  mgas  mstar  mbh  r  vmax
```

Here, `j` is a file-internal index running from 0 to $N-1$, `x`, `y`, `z` are the positional and `vx`, `vy`, `vz` the velocity coordinates of the subhalo `j`, and `mdm`, `mgas`, `mstar`, `mbh` denote its dark matter mass, baryonic mass, stellar mass and black hole mass, respectively. Point of reference for position and velocity is the central galaxy, which sits as subhalo with `j=0` in the origin of our frame of reference. The latter has been further rotated to align with the minor axis of the central.

This bulk information about all individual subhalos is preceded by some header information that yield properties pertaining to the whole of the halo:

```
1  #  fsub  N  M  R  x  y  z  vx  vy  vz  redshift
```

From those, we mainly use the number of subhalos `N` and the total halo mass `M` to complement the individual subhalo data.[2]

After reading the data in and separating and storing it appropriately, we proceed with some minor consistency checks, then iteratively compute possible three-satellite planes using a twice nested loop over all satellites except the central. Although we eliminate redundant parts of the loops, we must admit that this may in and by itself

---

[2]Please beware that in this specific section, N denotes the number of subhalos *including* the central, and not just the number of satellites as is the convention in the rest of this thesis.

be the single most inefficient step in our TSP implementation; it also happens to be very straight forward, though, and is a process that only needs to run exactly once for every data file. In the end, because of the $\mathcal{O}^3$ growth of TSPs described in Section 2.1.1, it is not the computational time that poses a bottleneck, but rather the memory available. In case the TSP method is pursued further, we will invest the necessary time to further optimize this segment of the process. One possibility is to store information on a grid at this point in the process already, necessitating an on the fly implementation.

The second to final step in layer 1 is the (quick) analysis of all TSP normal vectors against the minor axis of the central galaxy. This is computationally cheap – read the z component of the vector – due to Equation (2.6), and allows us to store the projected normal vector, which is exactly the $\cos\theta$ we will need later on, together with all the more detailed data in an output file.

The latter contains an expanded header that encompasses the original header of the input file with additional naming, but then also gives information about the number of three-satellite planes, how many had to be discarded (usually well below 0.1%) and then a large table with all computed TSPs represented by a new file-internal index, the original indices of the satellites constituting each plane, the three components of the general normal vector and the scalar value of the normal vector projected onto the central minor axis, and a marker if this specific plane should to be discarded in future processing.

Saving all of this data to the disk completes the first layer of the TSP implementation. Of course, all operations on objects of this class are performed by its own methods, allowing for clean and unambiguous handling.

Layer 2 - binning the data onto grids

The second layer centers around the `planesGrid` class. Its objects are created by reading in the output files of the previous section's `SHO` class objects, and they bin a specified reduction of the hugely memory consuming data onto fine grids of the users choosing. We decided for the detour of writing to and then reading again from disk instead of straight up integrating the binning into the `SHO` class, since our requirements for the grid files, for the specific axis of evaluation or any other parameter we did not deem important during the initial processing at layer 1 may change with time. The final design allows us to cut back on handling unnecessary data in the rest of the process, since we can easily bin again from the layer 1 output accordingly in the future.

In our specific use case, we selected a one-dimensional grid with 1000 bins to convert the different values of $\cos\theta$ into simple number counts per bin, and then write it to the disk, as well. Please consider that the largest layer 1 output file that

we produced has more than $4 \cdot 10^6$ lines of extensive information. The reduction to a grid output file of a mere thousand lines is enormous even for less extremely sized halos.

Layer 3 - creating grid collections and evaluating the data

The third layer focuses on grouping and then analyzing large numbers of grid files that have been produced in layer 2. To this end, we have designed a class called `Collection` and its sub-class `GridCollection`. For our current purposes, we have restricted ourselves to the use of `GridCollection`. At creation, the objects of this class read in a list of grid files that is handed to them by means of file names or entire directories, and make this data accessible to plotting and analysis methods.

Since we also defined basic operations like `__add__` and `__sub__` for the class, we can easily operate with several instances of them:

- `__add__`, which corresponds to the use of a + as operator between two `GridCollection` objects, returns a new object with all the grids of the second object that were not yet part of the first one added to it.

- `__sub__`, which corresponds to the use of a – as operator between two `GridCollection` objects, returns a new object with all the grids of the second object that were already part of the first one removed from it.

This enables the user to selectively reduce or expand the collection of grids and thus systems which he wants to analyze or compare. To further expand on these possibilities and to be able to put together collections according to user-specified parameters and not only by hand, we introduce an auxiliary class called `Criterium`, which then, as the name might suggest, enables you to define selection criteria – e.g. mass ranges, b-values, etc. – according to which the data set is (further) refined prior to final analysis.

In a final step, we plot the resulting histograms, in our case of $\cos \theta$ with respect to the spin minor axis of the central galaxy of each system.

3.2.2 The MTP implementation

Our implementation of the "momentum in thinnest plane" scheme differs from that of the previously described TSP scheme insofar as that the different steps described below are conducted right away on each halo, with the exception of the cumulative analysis of all halos that relies on the collected data.

Preparing for analysis

In preparation of the analysis, we set the accuracy described in Section 2.2.2 and invoke an according θ-ϕ array. We also pre-compute arrays of the respective sin( ) and cos( ), since they will be used multiple times for large numbers of evaluations later on. These arrays are read for evaluation only, data and results are stored in separate arrays.

Finding the thinnest planes

Next, we search for the thinnest plane of satellites in the halo, as described in Section 2.2.3. We compute the distances of all satellites in the system from all possible planes on the θ-ϕ grid and sort the results bottom to top. Then, for every number of satellites n between 2 and the total number N in the system, we compare distances and find the values (or rather array indices) of θ and ϕ that correspond to the $2, 3, \ldots, N$ smallest distances from the plane.

Computing the momentum in the plane

The momentum in these planes is not only computed analogously, but actually by the same routine just being handed the velocity instead of the positions as well as a different normalization constant. For all planes p_n, we proceed the same way, only that now η is stepping through all subset numbers in the range of $1, \ldots, n$. A mock-up example can be found in Table 2.3, and the results in Section 4.2.

Cumulative analysis

While each halo is being processed as described above, an independent routine that can be either enabled or disabled saves data-tuples of in-plane momentum fraction $F_{\{n\}}$, thickness fraction $D_{p,n}/2R_{\mathrm{halo}}$ and number of satellites n as well as some meta-information like total number of satellites N and the like to an individual output file per halo. Our specialized plotting routine then deals with the visualization of the data, allowing for flexible arrangements while still providing a solid framework. Please see Section 4.2.3 for the plots produced this way.

3.2.3 Plotting and other adventures

A substantial portion of the time and energy invested into this project as a whole went into minuscule routines that are either associated with visualization and then subsequent analysis and interpretation of the data, or that keep the major routines running and uncluttered. Typical examples from the latter category written specifically for this work include but are not limited to routines that

- change the working directory to the main file's directory to further on use relative paths without risk.

- retrieve a complete list of file names from a specified directory with the exception of hidden and system files, allowing for easy import of whole directories' worth of data.

- intelligently sort lists of objects.

- construct new file names automatically from e.g. plot titles while removing special characters and LATEXmathmode commands and substituting them with easily readable replacements.

The list could be extended near endlessly. But even if these routines may seem tiny and circumstantial at times, the author has learned to appreciate the readability and order they bring to a project as a whole and looks forward to reusing them in future projects.

4 Results

In this chapter, we present the results of our search for satellite planes in MAGNETICUM *Box4/uhr*. The first section contains the findings for "the three-satellites planes" (TSP) scheme described in Section 2.1, while the section after shows the results obtained with the "momentum in thinnest plane" (MTP) method of Section 2.2.

4.1 Results for the three-satellite planes scheme

We apply the three-satellite planes scheme to a large subset of our ensemble of halos. Due to computational reasons, we have to set a cut according to the number of satellites in a system, effectively resulting in a mass cut above $5.2 \cdot 10^{13} M_{\odot}$. This is caused by the $\mathcal{O}^3$ growth rate in number of TSPs for large numbers of satellites, as detailed in Section 2.1.1, Equations (2.1) and (2.2). Further optimization of the code or a substantial increase in available memory would push the limit for the number of satellites in a halo that can be analyzed further up.

For both analyses with the TSP scheme, we select the minor axis of the central galaxy of each halo as the axis of evaluation. This means that θ_{α} denotes the separation angle between the minor axis of the central, $\vec{c}$, and the normal vector of a plane of three satellites, $\vec{n}_{\alpha}$, according to Section 2.1.2, Equation (2.6).

4.1.1 b-value splits

In the first analysis with the three-satellite planes scheme, we divide our ensemble of halos into three groups according to the b-value (Teklu et al. 2015) of their central galaxies: our sample contains 129 disky centrals, 188 intermediate centrals, and 234 spheroidal centrals.

For each of the three galaxy types, figures 4.1 and 4.2 show the cumulative histograms of the probability density function (PDF) of the cosine of θ as described in Section 2.1.5, with all the PDFs of the according halos stacked. There, the light dashed line denotes the expected distribution of the cosine of the separation angle θ for a uniform (random) distribution of normal vectors in 3D space, while the dark dashed line marks the median of all systems in each separate bin. With regard to the latter, the dark shaded region bordered by the inner dotted lines covers $\pm 1\sigma \approx 68\%$, and the light shaded region bordered by the outer dotted lines covers $\pm 2\sigma \approx 95\%$
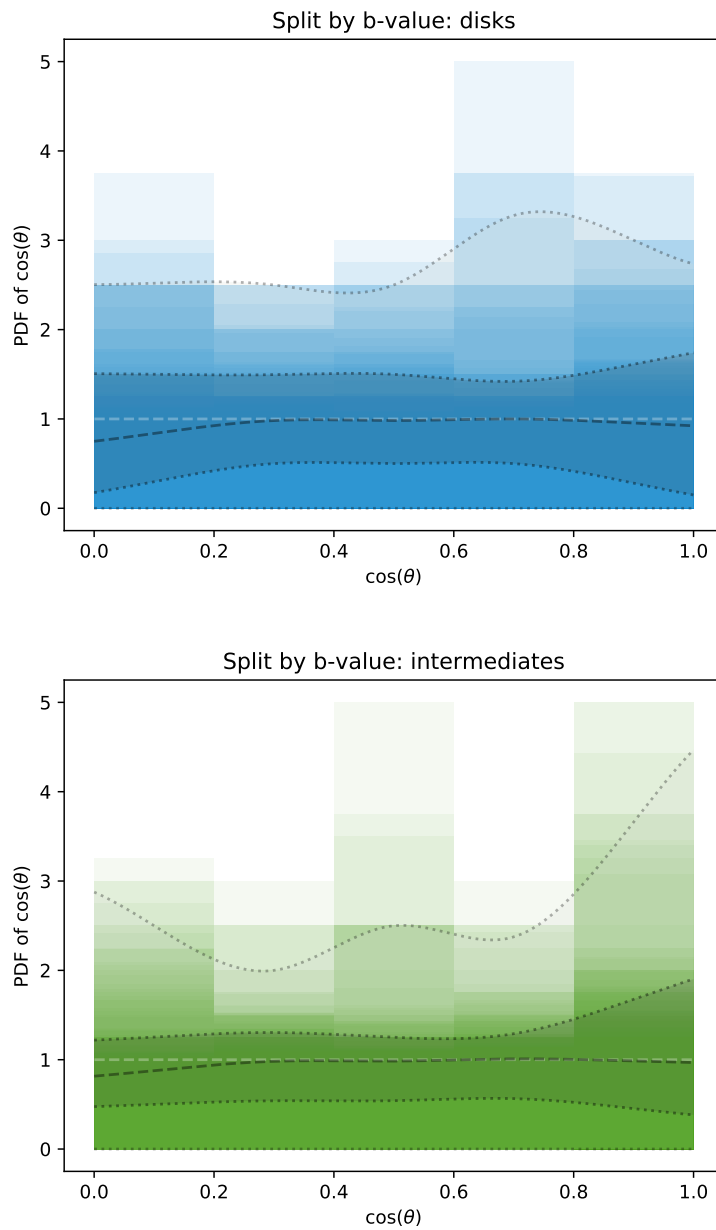
Figure 4.1: Stacked histograms of the probability density function (PDF) of $\cos\theta$ for all systems identified as containing one of the 129 disky (upper panel) or one of the 188 intermediate (lower panel) central galaxies, respectively. The light dashed line represents the uniform distribution on a sphere. The transparently grey shaded areas encompassed in dotted lines cover 1σ and 2σ of all selected systems, while the dark dashed line designates the median value of all systems, evaluated for each bin separately.
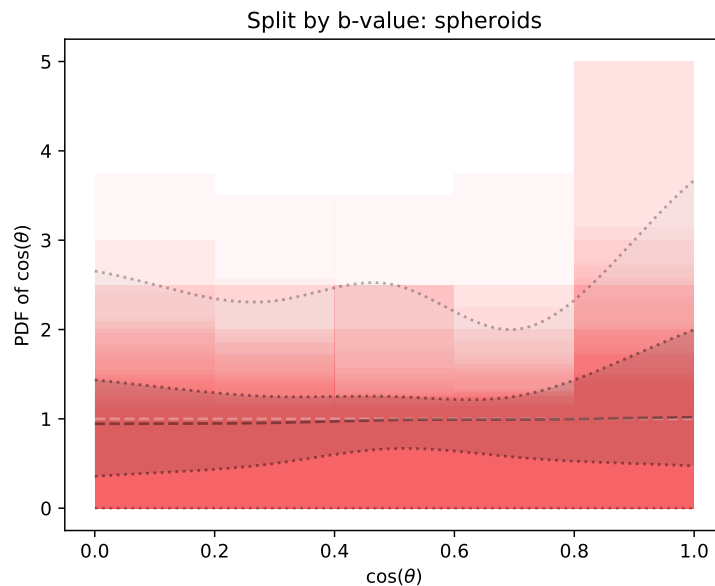
Figure 4.2: Stacked histograms of the probability density function (PDF) of $\cos\theta$ for all 234 systems identified as containing a spheroidal central galaxy. Please see Figure 4.1 for further description.

of all satellites in each selection. The transparent overlay of the histogram bars represents the number of systems with according probabilities in each bin – the darker and less transparent the shade, the more systems have at least this or a higher probability to find $\cos\theta$ in that bin.

Scatter in excess probability

In this analysis of our ensemble of halos with the TSP scheme, a slight trend in the $\cos\theta$ distribution is visible. The systems with disky central galaxies seem to disfavor values of $\cos\theta < 0.2$, a trend that is visible in the reduced median of the leftmost bin and that the intermediates share (Figure 4.1). On the other hand, systems of both spheroidal (Figure 4.2) and intermediate host galaxies display an increased scatter in the rightmost bin with $\cos\theta \leq 0.8$. The first trend indicates a decrease in excess probability of at most $\xi \approx 4\%$ for planes orthogonal to the disk of the central, while the latter indicates an increase of up to 14% of three-satellite planes that may roughly be aligned with the plane formed by the major and intermediate axis of the central galaxy.

Besides these two trends, we also observe a slight decrease in the general width of $\pm 1\sigma$ scatter, with the disks ($\xi_\pm \approx \pm 10\%$) at the upper and the spheroids ($\xi_+ \approx +6\%$, $\xi_- \approx -8\%$) at the lower end of this slight trend.

4.1.2 Total mass splits

In the second analysis with the TSP scheme, we divide our ensemble into three groups according to their total halo mass: our sample contains 124 halos of mass M below $10^{12} M_\odot$, 387 of mass between 10^{12} and $10^{13} M_\odot$, and 40 with a mass above $10^{13} M_\odot$.

For each of the three mass bins, figures 4.3 and 4.4 show the cumulative histograms of the probability density function (PDF) of the cosine of θ as described in Section 2.1.5, with all the PDFs of the according halos stacked. As in the previous section, the light dashed line denotes the expected distribution of the cosine of the separation angle θ for a uniform (random) distribution of normal vectors in 3D space, while the dark dashed line marks the median of all systems in each separate bin. With regard to the latter, the dark shaded region bordered by the inner dotted lines covers $\pm 1\sigma \approx 68\%$, and the light shaded region bordered by the outer dotted lines covers $\pm 2\sigma \approx 95\%$ of all satellites in each selection. The transparent overlay of the histogram bars represents the number of systems with according probabilities in each bin – the darker and less transparent the shade, the more systems have at least this or a higher probability to find $\cos\theta$ in that bin.

Scatter in excess probability

As opposed to the b-value separation of our galaxies, we see a clear distinction in the scatter of the excess probability ξ between the three mass bins: the lowest mass bin (Figure 4.3, upper panel) containing the 124 galaxy halos with $M < 10^{12} M_\odot$ has the largest scatter, with $\pm 1\sigma$ of systems showing excess probabilities between $\xi_- \approx [-16\%, -20\%]$ and $\xi_+ \approx [+17\%, +20\%]$ for the number of normal vector to minor axis separations angle cosines, $\cos\theta$; the mean value for each bin varies similarly.

The second mass bin encompasses all 387 galaxy halos with $10^{12} M_\odot \leq M < 10^{13} M_\odot$. The lower panel of Figure 4.3 shows significantly reduced scatter already, with the range of the excess probability of $\pm 1\sigma$ of these systems decreasing to $\xi_- \approx [-5\%, -10\%]$ and $\xi_+ \approx [+5\%, +13\%]$. This trend continues for the highest mass bin, with $\pm 1\sigma$ of all 40 halos in Figure 4.4 with $M \geq 10^{13} M_\odot$ showing a scatter of well below $\xi_\pm \lesssim \pm 3\%$. We will discuss possible explanations for this overall trend of TSP vs. halo mass anticorrelation in Section 5.1.1.

A tendency that holds up across both the splits into b-value bins and into mass bins is the slight preferment for a larger number of TSP to align with the disc (or equivalent) of the central galaxy.
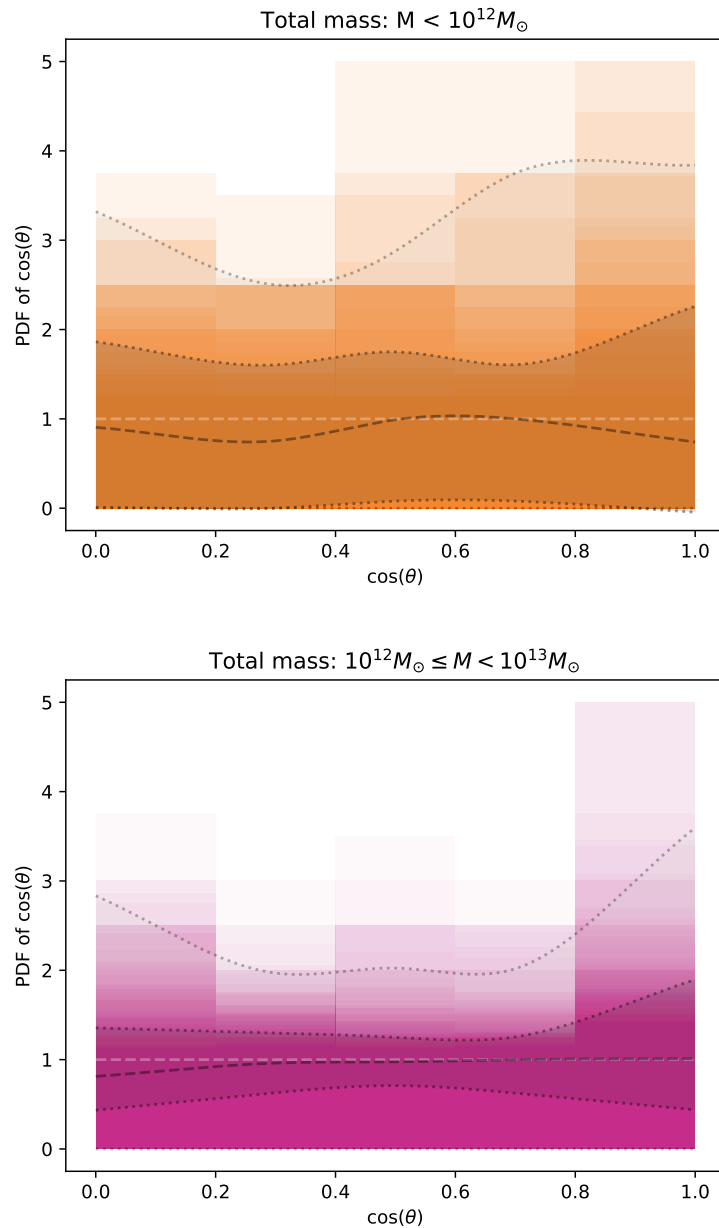
Figure 4.3: Stacked histograms of the probability density function (PDF) of $\cos\theta$ for the 124 systems with total halo mass $M < 10^{12}M_\odot$ (upper panel) and for the 387 systems with $10^{12}M_\odot \leq M < 10^{13}M_\odot$ (lower panel), respectively. The light dashed line represents the uniform distribution on a sphere. The transparently grey shaded areas encompassed in dotted lines cover 1σ and 2σ of all selected systems, while the dark dashed line designates the median value of all systems, evaluated for each bin separately.
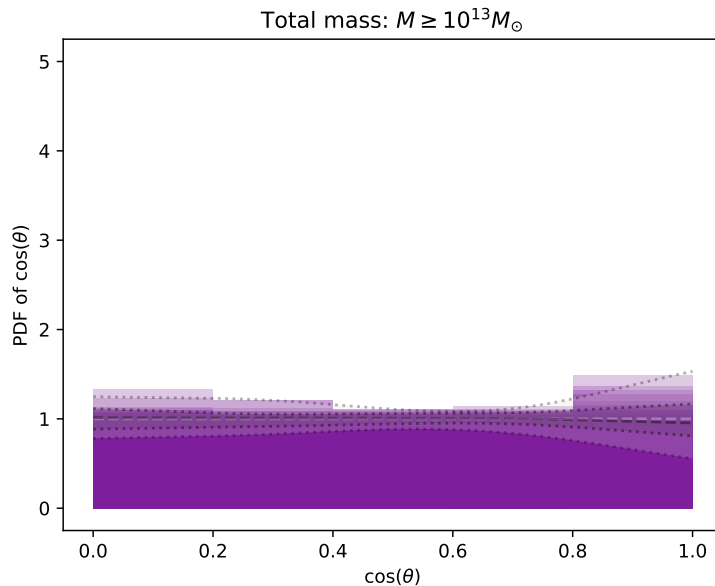
Figure 4.4: Stacked histograms of the probability density function (PDF) of $\cos\theta$ for all 40 systems with total halo mass $M \geq 10^{13}M_\odot$. Please see Figure 4.3 for further description.

4.2 Results for the momentum in thinnest planes scheme

Having presented the results of the three-satellites planes method in the previous section, we move on to the results of our analysis with the momentum in thinnest plane (MTP) method. We first take a brief look at typical thickness maps found while fitting the thinnest possible plane to the positions of subsets of the satellites of a system. In Section 4.2.2, we then examine the corresponding in-plane momentum of select systems in dependence of the number of satellites considered. Lastly, Section 4.2.3 shows cumulative plots of *all* systems in our ensemble, putting the three main quantities number of satellites n, plane thickness $D_{p,n}$ and in-plane momentum (fraction) $F_{\{n\}}$ into context with each other.

4.2.1 Thickness maps for select systems

The first step in our MTP analysis is finding the thinnest possible plane in a system containing both the central galaxy and a specified number of satellites, n. This is done by means of the Hesse normal form as described in Section 2.2.1 and following. In Figure 4.5, we show visualizations of the thinnest planes for the whole range of θ and ϕ value pairs on our grid, limited to halo 252 as an example.
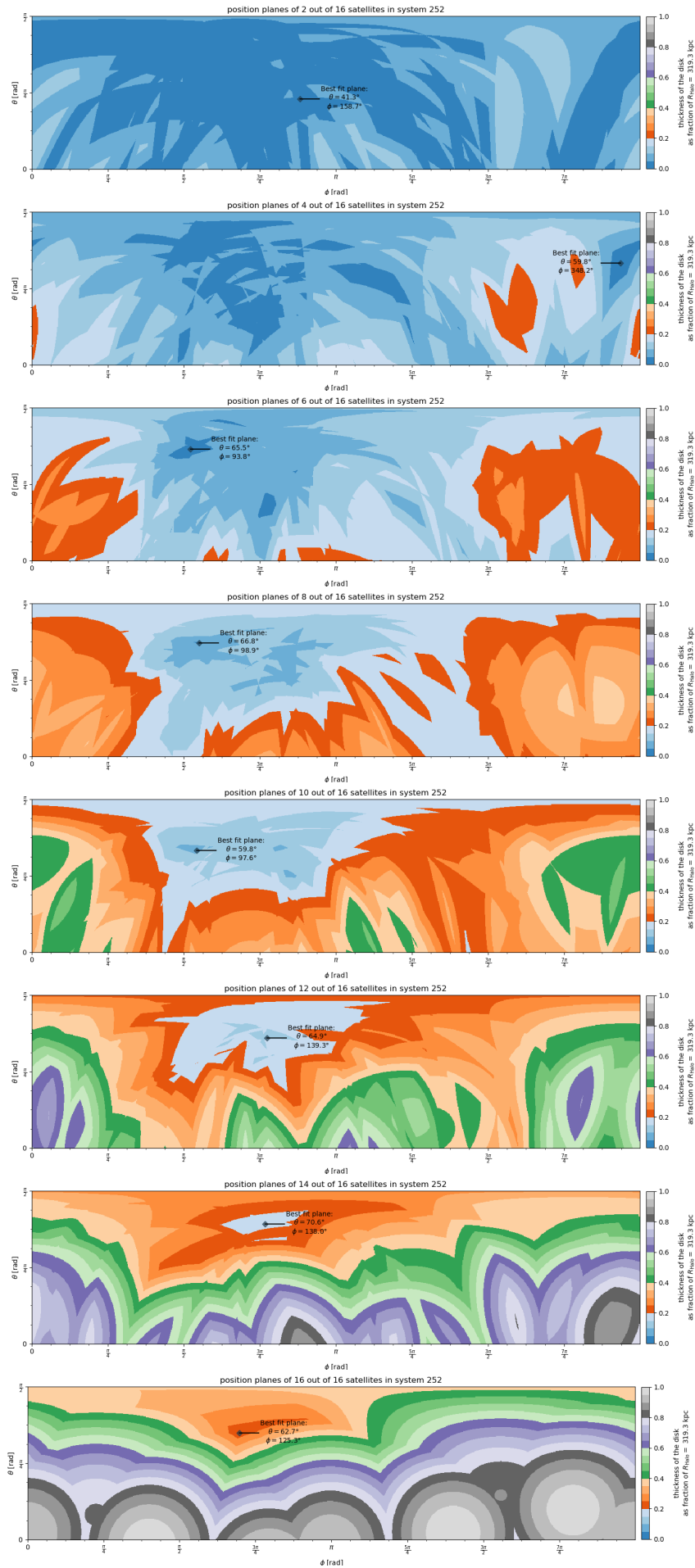
Figure 4.5: Thickness maps of halo 252 for planes fitted to increasing numbers of satellites, using the same color scheme as the momentum plots.

The eight panels of Figure 4.5 display the maps of the thicknesses of planes containing $n = 2, 4, \ldots, 16$ satellites (top to bottom). The angle θ is on the y- axis, while ϕ is on the x-axis. Shades of blue denote a thickness fraction of up to 20%, shades of red of up to 40%, shades of green of up to 60%, shades of violet of up to 80%, and shades of gray denote a thickness fraction of up to 100%. The same color scheme is used for the thickness fraction throughout this thesis, so that comparisons with single (Section 4.2) and cumulative (Figure 4.9) in-plane momentum plots are easily possible.

4.2.2 In-plane momentum for select systems

Following the fitting of the thinnest possible planes to any given number of satellites and the central, we use these minima to analyze the amount of momentum in direction of said plane according to Section 2.2.5, as this gives us a measure of the validity of the purely position-based fits in the previous section. Below, we present the results in form of plots displaying the in-plane momentum fraction $F_{\{\eta\}}$ for increasingly large subsets η of the number of satellites n used to fit the plane, with n in turn being an increasing subset of the total number of satellites of the system, N. For a schematic overview, consider an instance of Table 2.3 nested into each "$n = \ldots$" instance of Table 2.2.

A remark on the scope of the y-axes of the plots presented in this section: as per Equation (2.18), the momentum fraction in direction of a plane is equal to the fraction of momentum orthogonal to the plane for $F_{\{\eta\}} = \frac{1}{\sqrt{2}} \approx 0.7$. Since in-plane momenta of 70% or lesser of the total momentum therefore point to a configuration that is decidedly not moving in agreement with the position-wise fitted plane, we would gain no more information from the exact momentum fraction values than we do from the fact that they are below 0.7, and thus can focus our plots on the more relevant range of values.

Low- to intermediate mass halos with high in-plane momentum

In Figure 4.6, we present a lower mass halo hosting an intermediate central galaxy. Its total halo mass is $M = 8.65 \cdot 10^{11} M_{\odot}$, the number of satellites is $N = 6$. The halo shows consistently thin planes that also feature a high in-plane momentum fraction: the plane consisting of two thirds of the satellites has a thickness fraction of $D_{p,n}/2R_{\text{halo}} < 5\%$ and in-plane momentum of roughly $F_{\{n\}} = 95\%$ if all of its $n = 4$ satellites are considered , and even the plane consisting of all $N = 6$ satellites is below 10% in thickness and manages just below 94% in in-plane momentum.

Figure 4.7 shows two intermediate mass halos of similar behavior: halo 252, which we already encountered in form of its thickness maps in Figure 4.5, has a total mass of $M = 2.04 \cdot 10^{12} M_{\odot}$ and a spheroidal central galaxy, whereas halo 142 has a
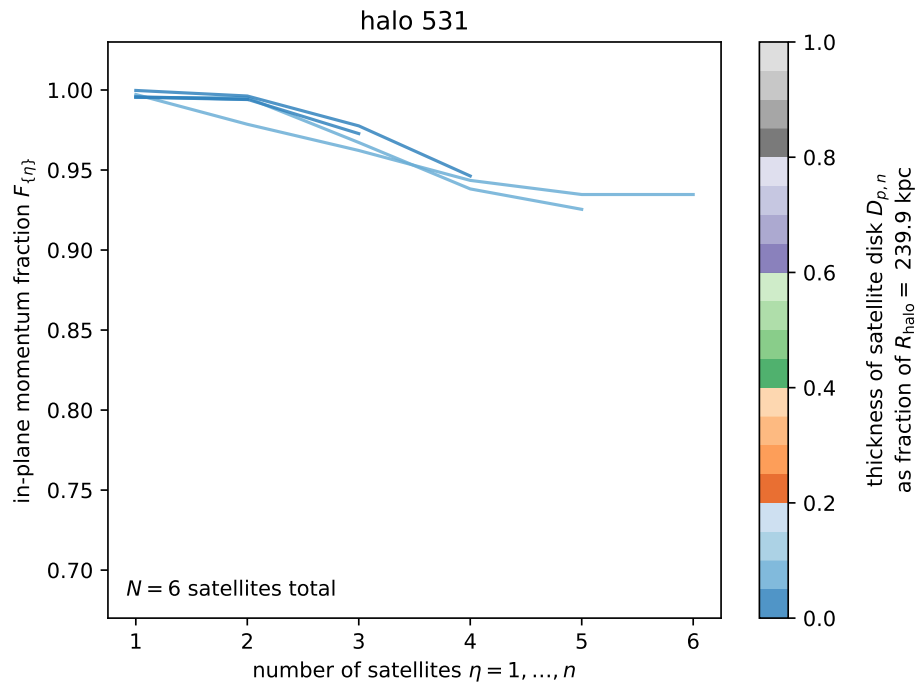
Figure 4.6: In-plane momentum fraction over number of satellites in planes of low-mass halo 531 with $M = 8.65 \cdot 10^{11} M_{\odot}$ and an intermediate central galaxy according to its b-value. The color-coding indicates the thickness of each fitted plane.
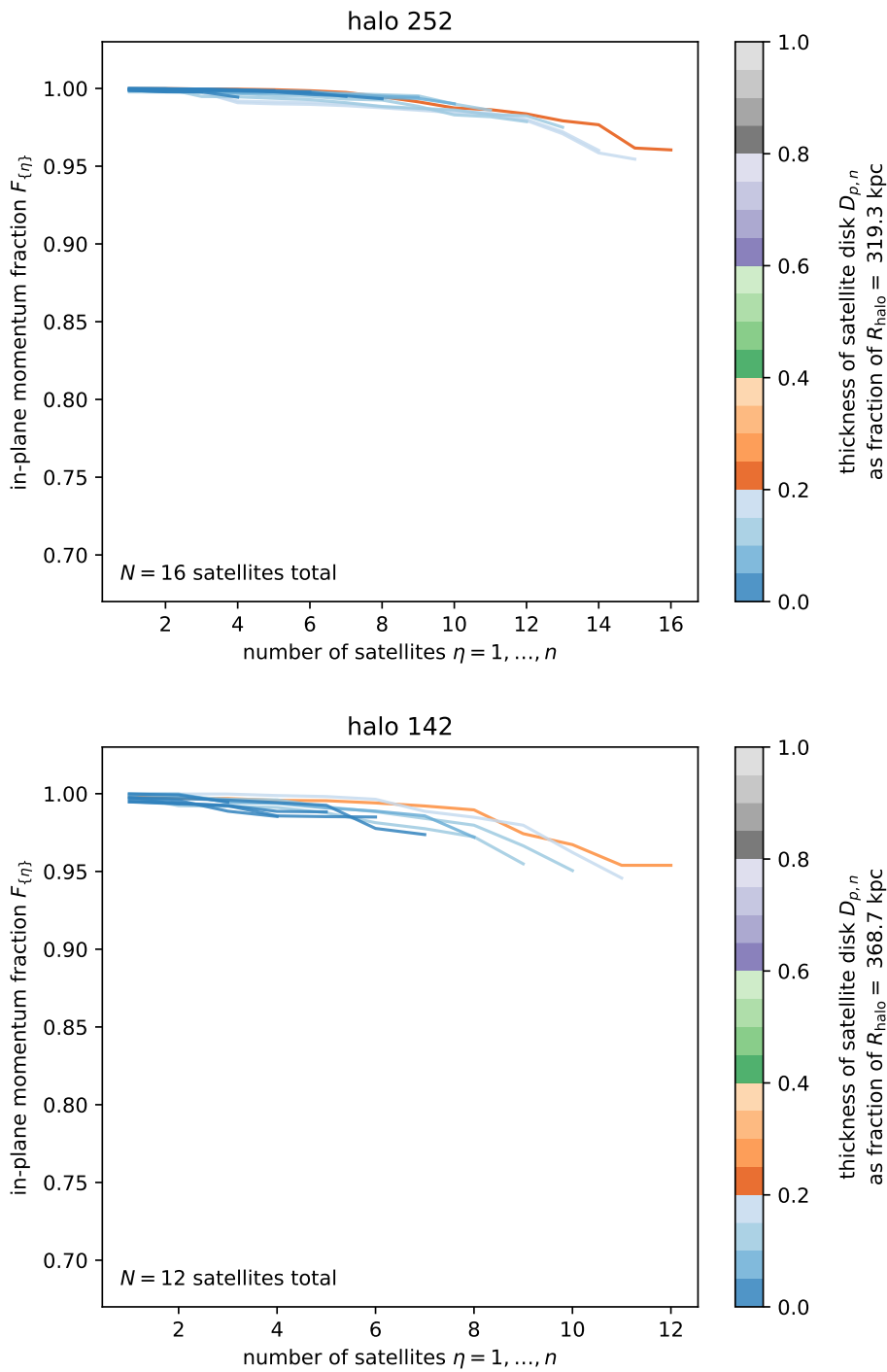
Figure 4.7: In-plane momentum fraction over number of satellites in planes of two intermediate-mass systems: halo 252 with $M = 2.04 \cdot 10^{12} M_\odot$ hosting a spheroidal central galaxy, and halo 142 with $M = 3.14 \cdot 10^{12} M_\odot$ hosting a central classified as disk by its b-value. The color-coding indicates the thickness of each fitted plane.

comparable mass of $M = 3.14 \cdot 10^{12} M_\odot$ and hosts a central classified as disk-type. Both generally stay above 95% of in-plane momentum, and for 80% of satellites in halo 252 and 67% of satellites in halo 142 they retain a very good $F_{\{\eta\}} \geq 97.5\%$. The plane thickness ranges up to a maximum of $D_{p,n}/2R_{\text{halo}} = 25\%$ and 30% for the all-satellite realization, respectively, but most their fitted planes stay under the 15% mark.

High-mass halos with different thickness and in-plane momentum

Figure 4.8 represents two distinctly different, high-mass systems: halo 608 ranges at $M = 1.70 \cdot 10^{14} M_\odot$ and is the second most massive halo in our ensemble of $\mathcal{N}_h = 622$ systems, while halo 613 is the sixth most massive with $M = 9.70 \cdot 10^{13} M_\odot$.

Halo 609 with its close to 900 satellites displays what might be expected of a massive intermediate with a halo full of virialized satellites: the higher the fraction of satellites involved in the fitting of the thinnest plane, the thicker and less momentum-aligned it becomes. It is interesting to note, though, that planes consisting of up to about 51% of all satellites lie above $F_{\{n\}} = 95\%$ and are quite thin at $D_{p,n}/2R_{\text{halo}} < 20\%$.

An even more extreme case presents itself with halo 613: albeit being home to 641 satellites, the massive halo with a disky central galaxy shows remarkably high and stable in-plane momentum. Except for one stray at about 91.5%, all realized planes lie above $F_{\{n\}} = 92.5\%$. It needs to be stressed that this is also true for the planes consisting of *all* or near to all satellites; albeit being considerably thicker and arguably not warranting the description of "plane" anymore, they share the overwhelming part of their momentum parallel to this plane.[1]

When thickness is taken into account, halo 613 displays even more remarkable features: up to 86% of its satellites move with about 96% of their momentum in a plane that is less than 40% in thickness compared to the extent of the halo. Those roughly 550 satellite constitute a significant plane in both position and momentum space.

4.2.3 Cumulative momentum in thinnest plane results

In this section, we will present the combined evaluation of all individual momentum in thinnest plane (MTP) results. To this end, we have accumulated the data equivalent to the endpoints of all $N - 1$ individual lines in the plots of Section 4.2.2 of *all* systems in our ensemble.

---

[1]The one comparably large "step" in many of the momentum-lines of halo 613 (Figure 4.8) may be attributed to a single or a very small number of satellites that do not preferentially move within the common plane. This would put the estimated quota for stray satellites at below 1%.
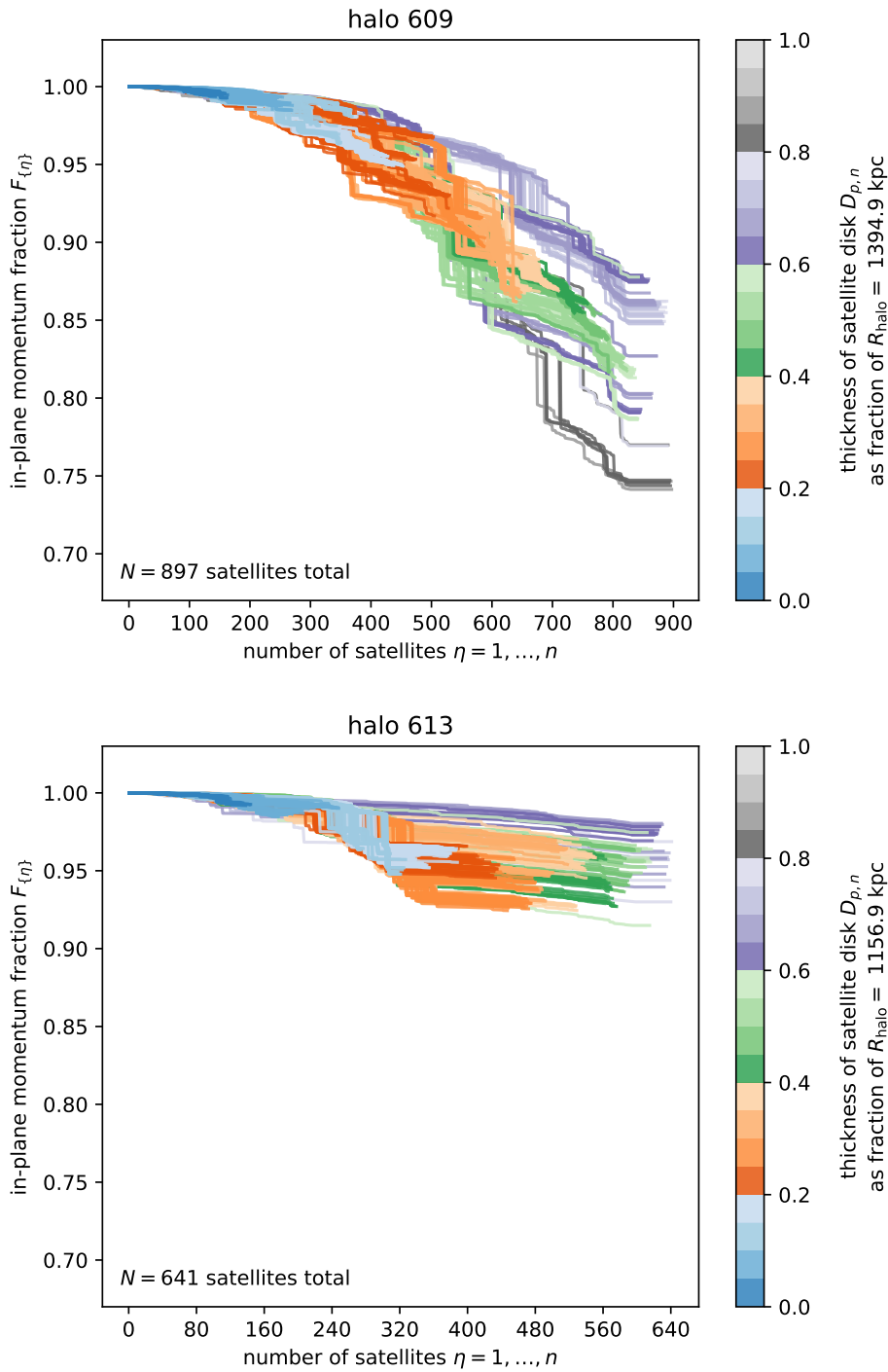
Figure 4.8: In-plane momentum fraction over number of satellites in planes of two high-mass systems: halo 609 with $M = 1.70 \cdot 10^{14} M_\odot$ hosting an intermediate central galaxy, and halo 613 with $M = 9.70 \cdot 10^{13} M_\odot$ hosting a central classified as disk by its b-value. The color-coding indicates the thickness of each fitted plane.

Thus, we obtain approximately $18,000$ data points, and each of them consists of three distinct pieces of information: the number of satellites n partaking in the complete position-wise fitted plane P_n, the thickness of said plane $D_{p,n}$, and the in-plane momentum fraction $F_{\{n\}}$ of all n satellites. From the original halo files, we further know the total number of satellites N and the radius of the whole halo R_{halo}, which we use to normalize the number of satellites in the plane and the thickness, respectively. The following sections place these quantities into different relations to each other.

In-plane momentum vs. fraction of satellites

Figure 4.9 is the direct, cumulative equivalent of the plots in Section 4.2.2, with all the endpoints of individual lines displayed as dots. The main panel shows the in-plane momentum fraction $F_{\{n\}}$ over the fraction of satellites of the system n/N that take part in the plane P_n, the thickness of which is color-coded as previously. There is a clear trend visible: our realizations of planes preferably fill the upper right half of the plot, which corresponds to a high in-plane momentum fraction. This trend is stronger for lower number of satellite fractions.

The histogram on top shows the distribution of the fraction of satellites n/N, and the color-coding reveals a somewhat expected preference of thinner disks on the lower end and thicker disks on the high end. The histogram to the right displays the distribution of satellites with respect to the in-plane momentum fraction, and here the trend towards the high values of $F_{\{n\}}$ is very pronounced: more than 40% of all realized planes P_n have 97.5% or more of their total momentum in direction of the plane, another 15% have an in-plane momentum of 95 to 97.5%. This indicates that more than 55% of all planes in our analysis consist of satellites in fair agreement with it motion-wise.[2] The color-coding further reveals that a very large percentage ($\approx 90\%$) of the aforementioned planes – or about 50% of planes total – are very thin with a thickness fraction $D_{p,n}/2R_{\text{halo}}$ below 20%.

In-plane momentum vs. thickness of plane

Figure 4.10 presents a way to assess how kinematically aligned the satellites of all realized planes are with respect to their thinnest fit planes, and puts it into relation with the individual planes' thickness. Therefore, the main panel shows the in-plane momentum fraction $F_{\{n\}}$ over the thickness fraction of the disks $D_{p,n}/2R_{\text{halo}}$. The fraction of satellites n/N is color-coded in bins of 10%. We see a very pronounced trend of plane realizations to cluster to the upper left corner of the panel.

---

[2]More specifically, it means that these position-wise fitted planes are not a chance fit of satellites moving in random directions that would not have been visible at a different point in near time.
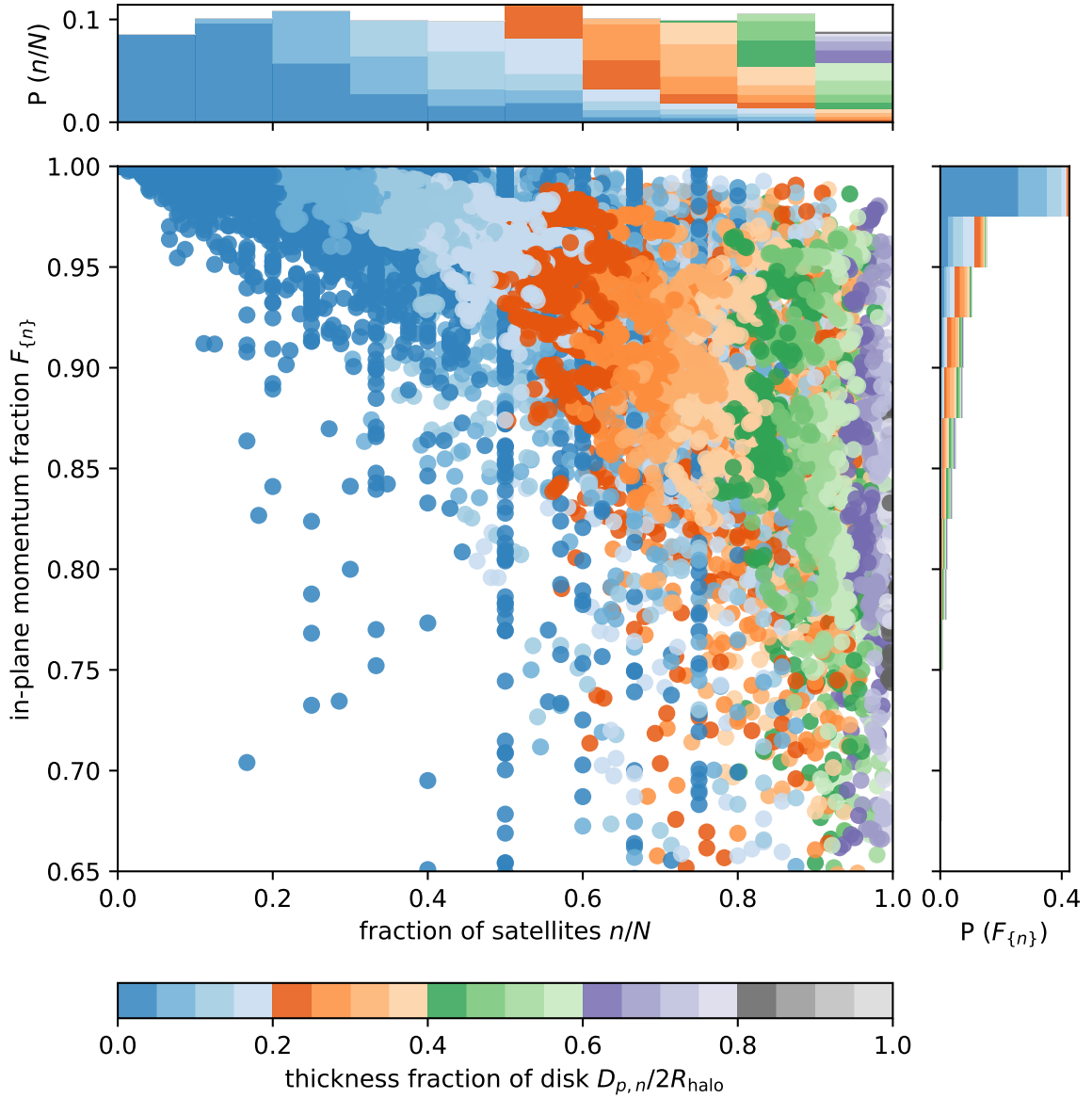
Figure 4.9: Cumulative plot of all systems: the in-plane momentum fraction $F_{\{n\}}$ over the fraction of satellites of the system n/N partaking in the plane P_n. Color-coded is the thickness of the plane as a fraction of the respective halo size $D_{p,n}/2R_{\text{halo}}$. The upper histogram shows the satellites' distribution in 10 n/N-bins, the right histogram their distribution in the 14 topmost of 40 $F_{\{n\}}$-bins. We limited the y-range of the plot as there are next to no data points with an in-plane momentum fraction below 0.65.
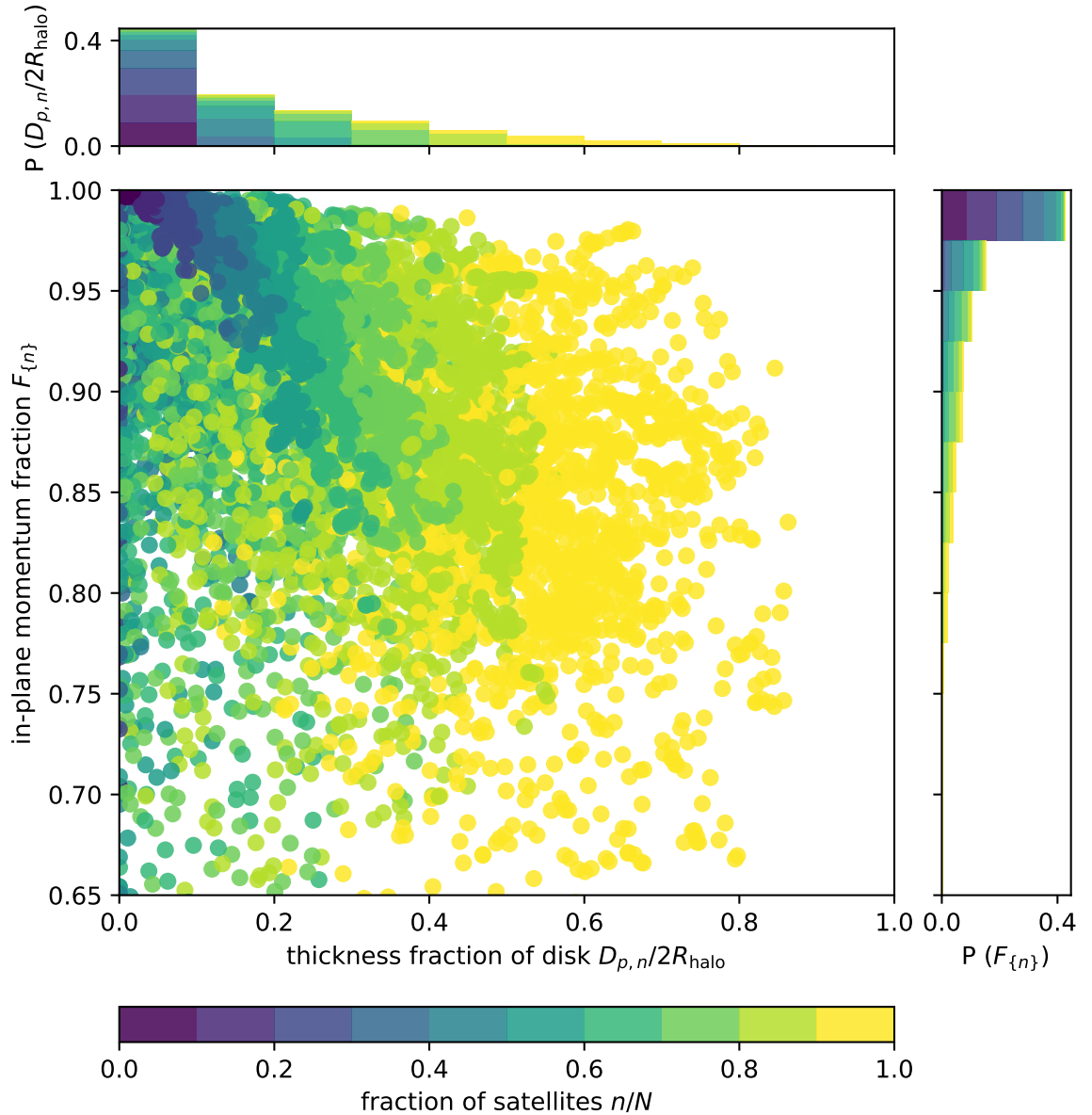
Figure 4.10: Cumulative plot of all systems: the in-plane momentum fraction $F_{\{n\}}$ over the thickness of the plane as a fraction of the respective halo size $D_{p,n}/2R_{\mathrm{halo}}$. Color-coded is the fraction of satellites of the system n/N partaking in the plane P_n. The upper histogram shows the satellites' distribution in 10 $D_{p,n}/2R_{\mathrm{halo}}$-bins, the right histogram their distribution in the 14 topmost of 40 $F_{\{n\}}$-bins. We limited the y-range of the plot as there are next to no data points with an in-plane momentum fraction below 0.65.

We learn from the top histogram that more than 40% of all planes consist of very thin disks with $D_{p,n}/2R_{\text{halo}} < 10\%$; combined with the planes of $10 - 20\%$ thickness, those planes amount to a good 60% of all planes. The histogram on the right-hand side then helps to specify how well within those planes the momentum of the partaking satellites lies: more than 40% of all planes have an in-plane momentum fraction above $F_{\{n\}} > 97.5\%$, an additional 16% lie in the next highest bin between 95% and 97.5%.

Combining both histograms and making use of their color-coding allows us to further narrow down on the composition of the most extremely clustered section in the top left corner of the main panel in Figure 4.10. Since about 80% of all planes with $n/N < 10\%$ and close to all planes with a number of satellites fraction between 10% and 20% percent are within the left-most and upper-most bins of the thickness and in-plane momentum histogram, respectively, we can assume that at least 17% of all realized planes lie in a portion of parameter space that makes up only 0.25% of it. The over-density can thus be deemed statistically significant.

Fraction of satellites vs. thickness of plane

Figure 4.11 completes our array of cumulative plots by showing the fractions of satellites n/N that are partaking in all best-fit planes P_n against the thickness fraction $D_{p,n}/2R_{\text{halo}}$ of said plane. The coloring shows different in-plane momenta. Since we learned from the right-hand side histograms of both previous Figures 4.9 and 4.10 that the fraction of planes with an in-plane momentum fraction below 70% is negligible, the color-coding is set up such that all $F_{\{n\}} < 65\%$ share a color. From there on, we use bins of 5%, which allows us to better differentiate in the more interesting scope of in-plane momentum.

Similar to previous plots, the top histogram shows the distribution of planes according to their thickness fraction $D_{p,n}/2R_{\text{halo}}$, while the right histogram represents their distribution with regard to the fraction of satellites n/N. We see from the color-coding that approximately 60% of all planes realized in our analysis have an in-plane momentum fraction of $F_{\{n\}} > 90\%$. These values' distribution favors the lower left side a bit, while higher, less kinetically coherent planes favor the upper middle section of the main panel.

The most striking feature of this figure is the huge, cleared area in satellite fraction vs. thickness fraction parameter space. It encompasses an estimated 60% of the panel, taking up the entire lower-right half of the plot and then some more. The implications of the lack of planes in this region of the plot will be discussed in Section 5.1.3.
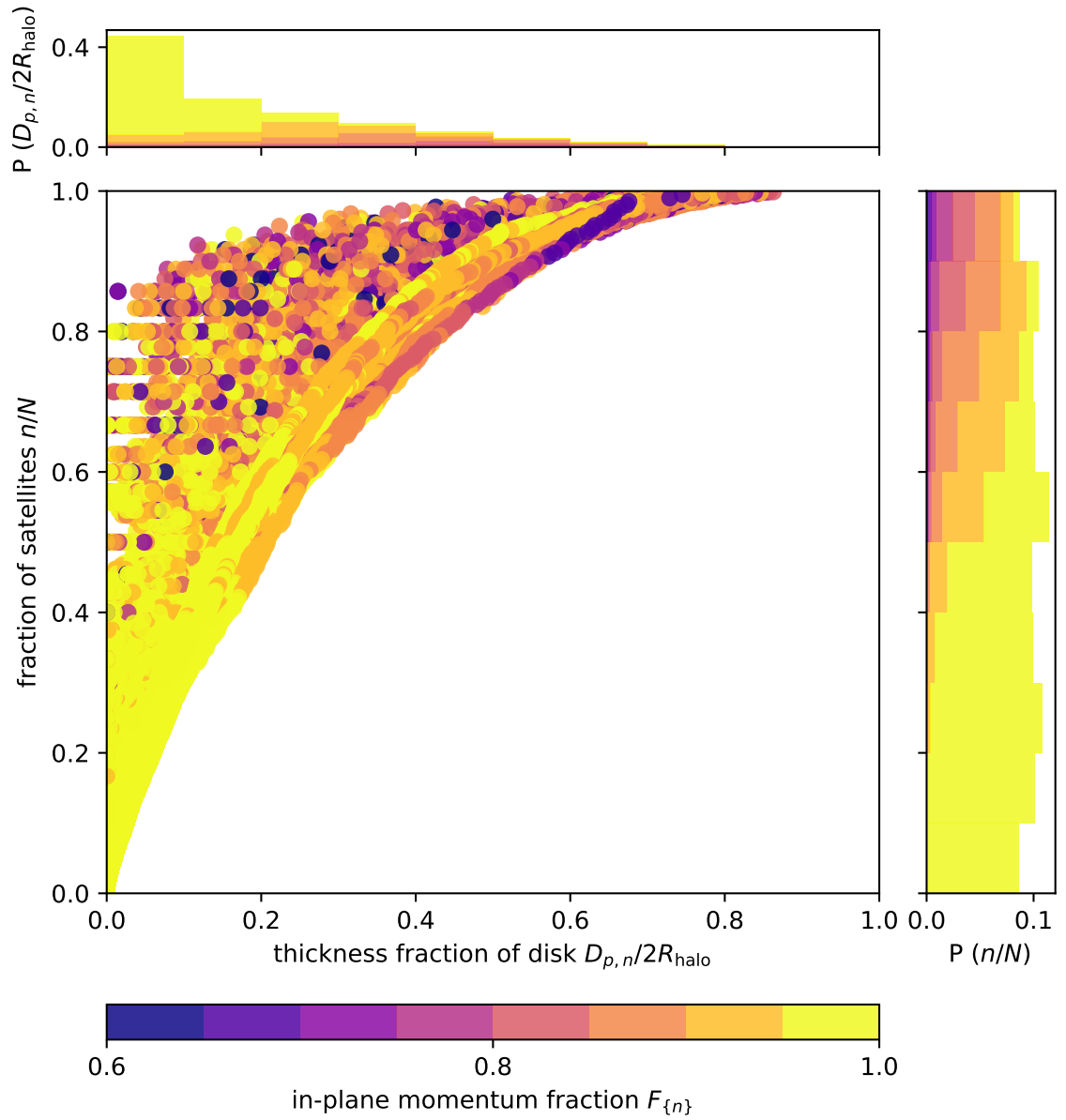
Figure 4.11: Cumulative plot of all systems: the fraction of satellites of the system n/N partaking in the plane P_n over the thickness of the plane as a fraction of the respective halo size $D_{p,n}/2R_{\text{halo}}$. Color-coded is the in-plane momentum fraction $F_{\{n\}}$. The upper histogram shows the satellites' distribution in 10 $D_{p,n}/2R_{\text{halo}}$-bins, the right histogram their distribution in the 10 n/N-bins.

5 Discussion

In this final chapter, we condense and analyze our previous findings. We furthermore sketch some ideas for future development of our methods and hint at their goals.

5.1 Conclusion

The results of our analysis in Chapter 4 have lead us to several conclusions about satellite planes in cosmological simulations in general and in MAGNETICUM in particular. We will consider the findings of both the TSP and the MTP scheme and weigh them against expectations and caveats.

5.1.1 Anticorrelation of TSP alignment and halo mass

The TSP analysis of our systems stacked in three groups with respect to their total halo mass in Section 4.1.2 yielded a clear result: while the systems in the lowest mass bin ($M < 10^{12}\,M_\odot$) show high scatter in the spread of the excess probability ξ, the scatter decreases for intermediate-mass halos ($10^{12}\,M_\odot \leq M < 10^{13}\,M_\odot$) and is near negligible at the high-mass end ($M \geq 10^{13}\,M_\odot$) of the systems analyzed via the three-satellite planes method.

The aforementioned, rather extreme scatter in ξ for $M < 10^{12}\,M_\odot$, as seen in the upper panel of Figure 4.1, may be attributed to the drastically smaller number of satellites associated with low-mass halos, as depicted in Figure 3.2. This in turn increases the scatter through noise, since the number of satellites can come uncomfortably near to the number of $\cos\theta$ bins. The steady decrease of ξ scatter with increase in total halo mass, as evidenced by Figure 4.1 (lower panel) and Figure 4.2, supports this conclusion.

Additionally, increasing numbers of satellites paired with higher masses point to halos that may have passed a phase in their evolution characterized by unidirectional accretion and are now subject to more isotropic infall. Since the TSP scheme does not take the movement of satellites into account, those massive systems would appear less prone to preferential alignment in our PDF histograms, nonetheless. This is different for the momentum in thinnest plane method, and we expand on that below.

5.1.2 Prevalence of thin sub-planes (MTP)

We identify two major reasons for the heavy preference ($> 40\%$) for very thin, momentum-aligned planes of satellites in the MTP scheme, corresponding to the first two bins of momentum fraction in Figure 4.9 and the first two thickness bins in both Figures 4.9 and 4.10, where $D_{p,n}/2R_{\mathrm{halo}} < 20\%$ and $F_{\{n\}} > 95\%$.

Probability considerations

Since we start fitting planes to subsets of the N subhalos of a system beginning from the smallest possible number of satellites $n = 2$, we find a lot of planes with $n/N < 0.5$ that are very thin. As a matter of fact, practically all planes below $n/N = 0.5$ are 20% in thickness or less, and about half of them are below 5% (cf. Figure 4.9). From a probabilistic approach, this is to be expected, since for some total number of satellites N, the chances to find $n < N$ of them in a plane of a certain thickness and thus volume becomes greater, the smaller that required subset of satellites is.[1]

A first approach might be to discard all planes that consist of less than maybe 30% of satellites of the whole halo. But we strongly discourage this for a reason that becomes apparent in Figure 4.10: a large number of plane realizations is located in the upper left corner of its main panel, pointing to very thin ($< 10\%$) and very kinematically coherent ($> 97, 5$) planes that to about two thirds consist of planes with $n/N < 0.3$. That those small-number sub-planes should be *both* thin and sport a high in-plane momentum with *exactly* this plane is non-trivial and may be a strong pointer to ordered infall or group accretion of a significant subset of the centrals' satellites. Here, the possible limitation of the MTP scheme by finding the thinnest planes of satellites solely by satellite position first, then checking their momentum-adherence turns out to be an advantage, since this minimizes the bias of those thin, coherent planes being "cherry picked" with regard to the momentum.

Formation history

Another reason to not dismiss these sub-planes is hidden in the fraction of n over N: we included a large scope of systems in our analysis, ranging from lower single digit numbers of satellites up to roughly a thousand. All three plots in Section 4.2.3 condense these three orders of magnitude down into one measure, the number of satellites fraction n/N, and thus favor the search for cosmological reasons independent of the actual size of any one galaxy system.

This notwithstanding, it could easily be argued that 30% of satellites of a system with order of 100 satellites are by themselves quite significant and – even if the

---

[1]As previously mentioned, this can nicely be seen in Figure 4.11.

coherent planes for this system do not consist of more than that – point to an earlier stage in the evolution of the halo where it mainly accreted dwarfs along the ridge of a filament, while at later stages of its evolution, when it presumably reached a node of the cosmic web, infall became multidirectional and the resulting satellite orientations more isotropic. This would be very much in line with the galaxy evolution scheme described in Section 1.2.1 and thus with expectations from ΛCDM.

5.1.3 Miscellaneous

The absolute lack of planes in the lower right region of Figure 4.11 (fraction of satellites vs. thickness fraction) provides us with confirmation that our search of thinnest possible planes over the whole range of satellite fractions is – at the very least – not unsuccessful or even conceptually flawed. Here is our reasoning: Finding the thinnest plane P_n corresponds to laying it through an overly dense region of the halo, or more specifically, to find the values for both angles θ and ϕ such that the density around the mathematical plane p_n is highest, with the constraint of exactly n satellites being in the volume extending $\pm d_n$ in either directions of p_n.

The lower boundary scenario for any number (fraction) of satellites n/N within a plane of thickness $D_{p,n}$ is then given by a halo with completely isotropically distributed satellites: there would be no overdensity to fit to, and the orientation of the plane would be mostly random.[2] This case is marked in Figure 4.11 by the planes sitting right on the border of the empty region.

All planes to the left and top of it represent overdense planes compared to the rest of the halo, and that the upper-left region beyond the parameter border is filled reasonably well speaks for the variety of our ensemble of systems. As to the nature of the "void": any hypothetical plane sitting in the empty region would represent an underdensity that we should not have fitted to in the first place, and that in turn would have introduced a corresponding overdensity for a differently oriented plane, which we then should have found instead.

5.2 Future prospects

We plan to additionally adopt some of the analysis techniques used by Müller et al. (2018) and others to quantitatively compare our findings to theirs. A direct comparison of our results from Section 4.2.3 with e.g. Figure 1.5 – and thus with both observations and other cosmological simulations – would be very desirable but sadly lies just beyond the scope of this thesis. Also, we did not (directly) check for co- and

---

[2]Finite numbers of satellites would nonetheless introduce a preference due to the non-continuous density associated with discrete particles.

counter-rotation of satellites around the central, especially not in spatially divided sections of the halo.

Concerning the more technical side of the methods of analysis we developed, we plan to implement some toy models for both the TSP and the MTP scheme to solidly test against statistical effects. Most of our results are – in our opinion – rather distinct and should not suffer too much from them.

Concerning MTP in particular, it might warrant the effort to further analyze (subsets) of the full in-plane momentum data we have, since we only used the momentum analysis of each full plane of satellites $F_{\{n\}}$ and not the information about its progenitors $F_{\{\eta\}}$ for the cumulative results. The current approach, though simpler, might involuntarily give some stray (pseudo-) satellites that happen to lie near the position-plane an unreasonable impact on the analysis' result.

Acknowledgments

This is the place to sincerely thank all the great people who helped and supported me over the course of my master's thesis:

PD Dr. Klaus Dolag and *Dr. Rhea-Silvia Remus*, for their great support and supervision, and for being as awesome as they are.

Prof. Dr. Andreas Burkert, for the numerous ideas and suggestions.

Adelheid Teklu, for providing data, help and insight.

Alexander Arth, for his support and understanding.

Johann Weber, for the fruitful discussions.

Ulrich Steinwandel and *Marcel Lotz*, for handing out good advice and asking hard questions.

Stefan, *Felix*, *Geray*, *Joe* and all the other great members of the CAST team and USM, for making this institute special.

My parents, for their love and patience.

Lidia, for simply being the best girlfriend between here and Andromeda.

And last but not least you, the reader, for perusing this master's thesis: Thank you!

<div align="right">

Munich, March 14, 2019
Pascal Ulrich Förster

</div>

Bibliography

Angus, G. W., Coppin, P., Gentile, G., and Diaferio, A. (2016). The potential role of NGC 205 in generating Andromeda's vast thin corotating plane of satellite galaxies. *Monthly Notices of the Royal Astronomical Society*, 462:3221–3242.

Beck, A. M., Murante, G., Arth, A., Remus, R.-S., Teklu, A. F., Donnert, J. M. F., Planelles, S., Beck, M. C., Förster, P., Imgrund, M., Dolag, K., and Borgani, S. (2016). An improved SPH scheme for cosmological simulations. *Monthly Notices of the Royal Astronomical Society*, 455:2110–2130.

Conn, A. R., Ibata, R. A., Lewis, G. F., Parker, Q. A., Zucker, D. B., Martin, N. F., McConnachie, A. W., Irwin, M. J., Tanvir, N., Fardal, M. A., Ferguson, A. M. N., Chapman, S. C., and Valls-Gabaud, D. (2012). A Bayesian Approach to Locating the Red Giant Branch Tip Magnitude. II. Distances to the Satellites of M31. *The Astrophysical Journal*, 758:11.

Dolag, K., Borgani, S., Murante, G., and Springel, V. (2009). Substructures in hydrodynamical cluster simulations. *Monthly Notices of the Royal Astronomical Society*, 399:497–514.

Dolag, K., Vazza, F., Brunetti, G., and Tormen, G. (2005). Turbulent gas motions in galaxy cluster simulations: the role of smoothed particle hydrodynamics viscosity. *Monthly Notices of the Royal Astronomical Society*, 364:753–772.

Dong, X. C., Lin, W. P., Kang, X., Ocean Wang, Y., Dutton, A. A., and Macciò, A. V. (2014). The Distribution of Satellites around Central Galaxies in a Cosmological Hydrodynamical Simulation. *The Astrophysical Journal*, 791:L33.

Foot, R. and Silagadze, Z. K. (2013). Thin disk of co-rotating dwarfs: A fingerprint of dissipative (mirror) dark matter? *Physics of the Dark Universe*, 2:163–165.

Hammer, F., Yang, Y., Fouquet, S., Pawlowski, M. S., Kroupa, P., Puech, M., Flores, H., and Wang, J. (2013). The vast thin plane of M31 corotating dwarfs: an additional fossil signature of the M31 merger and of its considerable impact in the whole Local Group. *Monthly Notices of the Royal Astronomical Society*, 431:3543–3549.

Ibata, R. A., Lewis, G. F., Conn, A. R., Irwin, M. J., McConnachie, A. W., Chapman, S. C., Collins, M. L., Fardal, M., Ferguson, A. M. N., Ibata, N. G., Mackey, A. D., Martin, N. F., Navarro, J., Rich, R. M., Valls-Gabaud, D., and Widrow,

L. M. (2013). A vast, thin plane of corotating dwarf galaxies orbiting the Andromeda galaxy. *Nature*, 493:62–65.

Kroupa, P. (2012). The Dark Matter Crisis: Falsification of the Current Standard Model of Cosmology. *Publications of the Astronomical Society of Australia*, 29:395–433.

Kroupa, P., Theis, C., and Boily, C. M. (2005). The great disk of Milky-Way satellites and cosmological sub-structures. , 431:517–521.

Kunkel, W. E. and Demers, S. (1976). The Magellanic Plane. In *The Galaxy and the Local Group*, volume 182, page 241.

Li, Y.-S. and Helmi, A. (2008). Infall of substructures on to a Milky Way-like dark halo. *Monthly Notices of the Royal Astronomical Society*, 385:1365–1373.

Libeskind, N. I., Frenk, C. S., Cole, S., Helly, J. C., Jenkins, A., Navarro, J. F., and Power, C. (2005). The distribution of satellite galaxies: the great pancake. *Monthly Notices of the Royal Astronomical Society*, 363:146–152.

Liddle, A. (2015). *An introduction to modern cosmology.* John Wiley & Sons.

Lynden-Bell, D. (1976). Dwarf galaxies and globular clusters in high velocity hydrogen streams. *Monthly Notices of the Royal Astronomical Society*, 174:695–710.

Lynden-Bell, D. and Lynden-Bell, R. M. (1995). Ghostly streams from the formation of the Galaxy's halo. *Monthly Notices of the Royal Astronomical Society*, 275:429–442.

McConnachie, A. W., Irwin, M. J., Ibata, R. A., Dubinski, J., Widrow, L. M., Martin, N. F., Côté, P., Dotter, A. L., Navarro, J. F., Ferguson, A. M. N., Puzia, T. H., Lewis, G. F., Babul, A., Barmby, P., Bienaymé, O., Chapman, S. C., Cockcroft, R., Collins, M. L. M., Fardal, M. A., Harris, W. E., Huxor, A., Mackey, A. D., Peñarrubia, J., Rich, R. M., Richer, H. B., Siebert, A., Tanvir, N., Valls-Gabaud, D., and Venn, K. A. (2009). The remnants of galaxy formation from a panoramic survey of the region around M31. *Nature*, 461:66–69.

Metz, M. and Kroupa, P. (2007). Dwarf spheroidal satellites: are they of tidal origin? *Monthly Notices of the Royal Astronomical Society*, 376:387–392.

Metz, M., Kroupa, P., Theis, C., Hensler, G., and Jerjen, H. (2009). Did the Milky Way Dwarf Satellites Enter The Halo as a Group? *The Astrophysical Journal*, 697:269–274.

Müller, O., Jerjen, H., and Binggeli, B. (2017). New low surface brightness dwarf galaxies in the Centaurus group. , 597:A7.

Müller, O., Jerjen, H., Pawlowski, M. S., and Binggeli, B. (2016). Testing the two planes of satellites in the Centaurus group. , 595:A119.

Müller, O., Pawlowski, M. S., Jerjen, H., and Lelli, F. (2018). A whirling plane of satellite galaxies around Centaurus A challenges cold dark matter cosmology. *Science*, 359:534–537.

Nichols, M., Colless, J., Colless, M., and Bland -Hawthorn, J. (2011). Accretion of the Magellanic System onto the Galaxy. *The Astrophysical Journal*, 742:110.

Pawlowski, M. S. (2016). The alignment of SDSS satellites with the VPOS: effects of the survey footprint shape. *Monthly Notices of the Royal Astronomical Society*, 456:448–458.

Pawlowski, M. S. (2018). The planes of satellite galaxies problem, suggested solutions, and open questions. *Modern Physics Letters A*, 33:1830004.

Pawlowski, M. S., Famaey, B., Jerjen, H., Merritt, D., Kroupa, P., Dabringhausen, J., Lüghausen, F., Forbes, D. A., Hensler, G., Hammer, F., Puech, M., Fouquet, S., Flores, H., and Yang, Y. (2014). Co-orbiting satellite galaxy structures are still in conflict with the distribution of primordial dwarf galaxies. *Monthly Notices of the Royal Astronomical Society*, 442:2362–2380.

Pawlowski, M. S. and McGaugh, S. S. (2014). Co-orbiting Planes of Sub-halos are Similarly Unlikely around Paired and Isolated Hosts. *The Astrophysical Journal*, 789:L24.

Pawlowski, M. S., Pflamm-Altenburg, J., and Kroupa, P. (2012). The VPOS: a vast polar structure of satellite galaxies, globular clusters and streams around the Milky Way. *Monthly Notices of the Royal Astronomical Society*, 423:1109–1126.

Ploeckinger, S., Sharma, K., Schaye, J., Crain, R. A., Schaller, M., and Barber, C. (2018). Tidal dwarf galaxies in cosmological simulations. *Monthly Notices of the Royal Astronomical Society*, 474:580–596.

Ragagnin, A., Dolag, K., Biffi, V., Cadolle Bel, M., Hammer, N. J., Krukau, A., Petkova, M., and Steinborn, D. (2017). A web portal for hydrodynamical, cosmological simulations. *Astronomy and Computing*, 20:52–67.

Randall, L. and Scholtz, J. (2015). Dissipative dark matter and the Andromeda plane of satellites. *Journal of Cosmology and Astro-Particle Physics*, 2015:057.

Romanowsky, A. J. and Fall, S. M. (2012). Angular Momentum and Galaxy Formation Revisited. *Astrophysical Journal Supplement Series*, 203:17.

Shao, S., Cautun, M., Frenk, C. S., Grand , R. J. J., Gómez, F. A., Marinacci, F., and Simpson, C. M. (2018). The multiplicity and anisotropy of galactic satellite accretion. *Monthly Notices of the Royal Astronomical Society*, 476:1796–1810.

Springel, V. (2005). The cosmological simulation code GADGET-2. *Monthly Notices of the Royal Astronomical Society*, 364:1105–1134.

Springel, V., White, S. D. M., Tormen, G., and Kauffmann, G. (2001). Populating a cluster of galaxies - I. Results at z=0. *Monthly Notices of the Royal Astronomical Society*, 328:726–750.

Teklu, A. F. (2018). *A dress code for galaxies: how the interplay of gas, stars, dark matter and environment shapes their appearance in simulations*. PhD thesis, Ludwig-Maximilians-Universität, München.

Teklu, A. F., Remus, R.-S., Dolag, K., Beck, A. M., Burkert, A., Schmidt, A. S., Schulze, F., and Steinborn, L. K. (2015). Connecting Angular Momentum and Galactic Dynamics: The Complex Interplay between Spin, Mass, and Morphology. *The Astrophysical Journal*, 812:29.

The Dark Energy Survey Collaboration (2005). The Dark Energy Survey. *arXiv e-prints*, pages astro–ph/0510346.

Tully, R. B., Libeskind, N. I., Karachentsev, I. D., Karachentseva, V. E., Rizzi, L., and Shaya, E. J. (2015). Two Planes of Satellites in the Centaurus A Group. *The Astrophysical Journal*, 802:L25.

Wang, J., Frenk, C. S., and Cooper, A. P. (2013). The spatial distribution of galactic satellites in the Λ cold dark matter cosmology. *Monthly Notices of the Royal Astronomical Society*, 429:1502–1513.

Weilbacher, P. M., Duc, P. A., Fritze v. Alvensleben, U., Martin, P., and Fricke, K. J. (2000). Tidal dwarf candidates in a sample of interacting galaxies. , 358:819–834.

Welker, C., Dubois, Y., Pichon, C., Devriendt, J., and Chisari, N. E. (2018). Caught in the rhythm. I. How satellites settle into a plane around their central galaxy. , 613:A4.

Welker, C., Power, C., Pichon, C., Dubois, Y., Devriendt, J., and Codis, S. (2017). Caught in the rhythm II: Competitive alignments of satellites with their inner halo and central galaxy. *arXiv e-prints*, page arXiv:1712.07818.

Wetzel, A. R., Deason, A. J., and Garrison-Kimmel, S. (2015). Satellite Dwarf Galaxies in a Hierarchical Universe: Infall Histories, Group Preprocessing, and Reionization. *The Astrophysical Journal*, 807:49.

Wetzstein, M., Naab, T., and Burkert, A. (2007). Do dwarf galaxies form in tidal tails? *Monthly Notices of the Royal Astronomical Society*, 375:805–820.

York, D. G., Adelman, J., Anderson, John E., J., Anderson, S. F., Annis, J., Bahcall, N. A., Bakken, J. A., Barkhouser, R., Bastian, S., Berman, E., Boroski, W. N., Bracker, S., Briegel, C., Briggs, J. W., Brinkmann, J., Brunner, R., Burles, S., Carey, L., Carr, M. A., Castander, F. J., Chen, B., Colestock, P. L., Connolly, A. J., Crocker, J. H., Csabai, I., Czarapata, P. C., Davis, J. E., Doi, M., Dombeck, T., Eisenstein, D., Ellman, N., Elms, B. R., Evans, M. L., Fan, X., Federwitz,

G. R., Fiscelli, L., Friedman, S., Frieman, J. A., Fukugita, M., Gillespie, B., Gunn, J. E., Gurbani, V. K., de Haas, E., Haldeman, M., Harris, F. H., Hayes, J., Heckman, T. M., Hennessy, G. S., Hindsley, R. B., Holm, S., Holmgren, D. J., Huang, C.-h., Hull, C., Husby, D., Ichikawa, S.-I., Ichikawa, T., Ivezić, Ž., Kent, S., Kim, R. S. J., Kinney, E., Klaene, M., Kleinman, A. N., Kleinman, S., Knapp, G. R., Korienek, J., Kron, R. G., Kunszt, P. Z., Lamb, D. Q., Lee, B., Leger, R. F., Limmongkol, S., Lindenmeyer, C., Long, D. C., Loomis, C., Loveday, J., Lucinio, R., Lupton, R. H., MacKinnon, B., Mannery, E. J., Mantsch, P. M., Margon, B., McGehee, P., McKay, T. A., Meiksin, A., Merelli, A., Monet, D. G., Munn, J. A., Narayanan, V. K., Nash, T., Neilsen, E., Neswold, R., Newberg, H. J., Nichol, R. C., Nicinski, T., Nonino, M., Okada, N., Okamura, S., Ostriker, J. P., Owen, R., Pauls, A. G., Peoples, J., Peterson, R. L., Petravick, D., Pier, J. R., Pope, A., Pordes, R., Prosapio, A., Rechenmacher, R., Quinn, T. R., Richards, G. T., Richmond, M. W., Rivetta, C. H., Rockosi, C. M., Ruthmansdorfer, K., Sandford, D., Schlegel, D. J., Schneider, D. P., Sekiguchi, M., Sergey, G., Shimasaku, K., Siegmund, W. A., Smee, S., Smith, J. A., Snedden, S., Stone, R., Stoughton, C., Strauss, M. A., Stubbs, C., SubbaRao, M., Szalay, A. S., Szapudi, I., Szokoly, G. P., Thakar, A. R., Tremonti, C., Tucker, D. L., Uomoto, A., Vanden Berk, D., Vogeley, M. S., Waddell, P., Wang, S.-i., Watanabe, M., Weinberg, D. H., Yanny, B., Yasuda, N., and SDSS Collaboration (2000). The Sloan Digital Sky Survey: Technical Summary. *Astronomical Journal*, 120:1579–1587.

Zentner, A. R., Kravtsov, A. V., Gnedin, O. Y., and Klypin, A. A. (2005). The Anisotropic Distribution of Galactic Satellites. *The Astrophysical Journal*, 629:219–232.

List of Figures

List of Tables

Selbstständigkeitserklärung

Hiermit erkläre ich, die vorliegende Arbeit selbständig verfasst zu haben und keine anderen als die in der Arbeit angegebenen Quellen und Hilfsmittel benutzt zu haben.

München, den 14. März 2019

Ort, Datum

Unterschrift